J. Fluid Mech. (2004), *vol.* 516, *pp.* 1–37.
DOI: 10.1017/S0022112004000357 Printed in the United Kingdom

The influence of non-equilibrium dissociation on the flow produced by shock impingement on a blunt body

By S. R. SANDERSON†, H. G. HORNUNG AND B. STURTEVANT‡

Graduate Aeronautical Laboratories, California Institute of Technology, Pasadena, CA 91125, USA

(Received 20 November 2003 and in revised form 11 May 2004)

We describe an investigation of the effects of non-equilibrium thermochemistry on the interaction between a weak oblique shock and the strong bow shock formed by a blunt body in hypersonic flow. This type of shock-on-shock interaction, also known as an Edney type IV interaction, causes locally intense enhancement of the surface heat transfer rate. A supersonic jet is formed by the nonlinear interaction that occurs between the two shock waves and elevated heat transfer rates and surface pressures are produced by the impingement of the supersonic jet on the body. The current paper is motivated by previous studies suggesting that real gas effects would significantly increase the severity of the phenomenon.

Experiments are described in which a free-piston shock tunnel is used to produce shock interaction flows with significant gas dissociation. Surprisingly, the data that are obtained show no significant stagnation enthalpy dependence of the ratio of the peak heat transfer rates with and without shock interaction, in contrast to existing belief. The geometry investigated is the nominally two-dimensional flow about a cylinder with coplanar impinging shock wave. Holographic interferometry is used to visualize the flow field and to quantify increases in the stagnation density caused by shock interaction. Time-resolved heat transfer measurements are obtained from surface junction thermocouples about the model forebody.

An improved model is developed to elucidate the finite-rate thermochemical processes occurring in the interaction region. It is shown that severe heat transfer intensification is a result of a jet shock structure that minimizes the entropy rise of the supersonic jet fluid whereas strong thermochemical effects are promoted by conditions that maximize the entropy rise (and hence temperature). This dichotomy underlies the smaller than anticipated influence of real gas effects on the heat transfer intensification. The model accurately predicts the measured heat transfer rates.

Improved understanding of the influence of real gas effects on the shock interaction phenomenon reduces a significant element of risk in the design of hypersonic vehicles. The peak heat transfer rate for the Edney type IV interaction is shown to be well-correlated, in the weak impinging shock regime, by an expression of the form $(\hat{q}-1)\approx 1+\phi_0(M_\infty-1)^{\phi_1}\delta_1^{\phi_2}$ for use in practical design calculations.

---

† Present address: GE Corporate Research & Development, 1 Research Circle, Niskayuna, NY 12309, USA.

‡ Professor Sturtevant died on 20 October 2000 during the preparation of this paper.

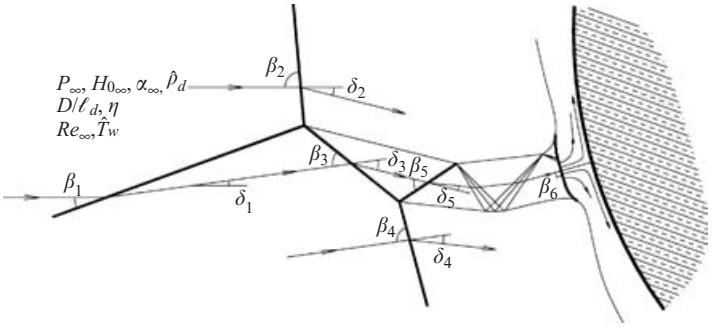

FIGURE 1. Schematic of the type IV shock interference flow field. The free-stream parameters for the case of an ideal dissociating gas are defined in § 6. For a perfect gas this set of parameters reduces to M_∞ and γ.

1. Introduction

1.1. *Motivation*

The interaction of a weak oblique shock wave with the bow shock ahead of a blunt body in steady supersonic flow is known to cause extremely high local heat transfer rates and surface pressures Edney (1968*a*, *b*). This phenomenon represents a severe constraint on the design of hypervelocity vehicles. Korkegi (1971) has conducted an extensive review of the broader shock wave interaction literature and discusses the available data from flight test vehicles. The phenomenon is observed in vehicles with a delta planform where the bow shock intersects the swept leading edge of the wing, in flow paths of supersonic propulsion systems and in the complex interaction flow fields that arise between supersonic vehicles and externally mounted tanks or boosters. Vehicles such as these operate in regimes that produce significant departures from thermochemical equilibrium in the flow about vehicle surfaces. The influences of real gas effects on this design-limiting phenomenon are hitherto poorly understood.

1.2. *Description of the phenomenon*

The most complete description of the shock impingement phenomenon is due to Edney (1968*a*) who observed and classified six distinct interaction regimes known as types I–VI. Keyes & Hains (1973) report additional experiments and parametric studies that further advanced the fundamental work of Edney (1968*a*). Keyes & Hains (1973) also review some of the earliest investigations that provided flow visualization and surface measurements for a variety of configurations but failed to elucidate the fundamental mechanisms of the problem. Severe heating occurs when the incident shock wave impinges in the vicinity of the geometrical stagnation point and a type IV flow results. Our discussion will concentrate on the type IV flow since the heating rates for the remaining regimes are less intense and therefore not design limiting.

Figure 1 shows the physical model of the flow field that was originally proposed by Edney (1968*a*). The main features of the type IV interaction may be discerned in figure 8 below. A three-shock λ-pattern is observed at the point where the impinging shock wave, 1, interacts with the bow shock, 2. A strong vortex sheet emanates from the λ-point. The shock layer flow above the vortex sheet is subsonic whereas the flow between the vortex sheet and reflected shock wave, 3, remains supersonic. A second, less distinct, inverted λ-pattern is observed at the intersection between the reflected shock, 3, and the continuation of the strong bow shock below the interaction region, 4. An additional oblique wave, 5, is reflected upwards at the secondary λ-point and a

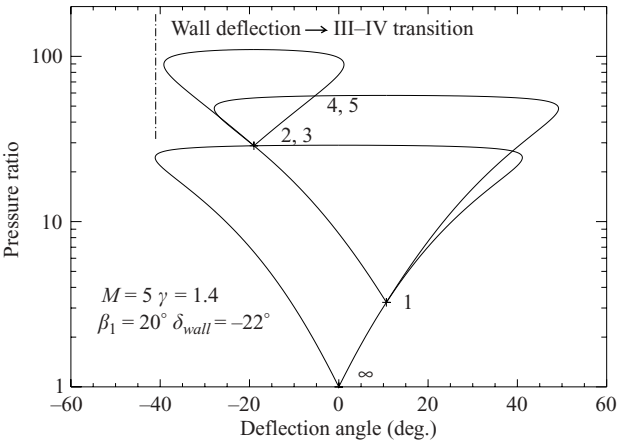

FIGURE 2. Representation of the type IV shock interference flow field in the (p, δ)-plane.

second vortex sheet is produced. Observe that the two vortex sheets bound a supersonic jet that is embedded in the surrounding subsonic shock layer. The jet is formed from the fluid passing between the two λ-points. The oblique wave, 5, crossing the jet is guided along the supersonic jet by successive reflections from the two shear layers. A strong terminating shock, 6, is observed at the base of the jet. The two shear layers turn rapidly upward and downward respectively with the strong pressure differential across the terminating shock being balanced by extreme streamline curvature. Additional shock structures may be present in the outflow to either side of the terminating shock; however it is not possible to conclusively categorize such structures based on the experimental results described here. The entire inviscid jet structure described above is gradually consumed by the spreading of the two shear layers that entrain the subsonic shock layer fluid into the supersonic jet.

1.3. *Inviscid jet flow field model*

Considerable insight may be obtained by mapping the flow field in the vicinity of the shock wave intersection points into the pressure–flow deflection angle (p, δ)-plane (details of the method are well known in the study of Mach reflection phenomena (e.g. Courant & Friedrichs 1948; Hornung 1986)). The (p, δ)-plane solution that is valid in the immediate vicinity of the two type IV interaction λ-points is shown in figure 2. The important conclusion to be drawn from figure 2 is that given only the free-stream Mach number, M_∞, the ratio of specific heats for the gas, γ, and the incident shock angle, β_1, the intersection of the loci representing states 2 and 3 in figure 2 completely determines all of the wave angles and flow properties at the shock impingement point. Since this fixes the strength of the wave, 3, that connects the two λ-points, the solution at the second inverted λ-point is also completely determined. The same (p, δ)-plane methods also allow prediction of the subsequent reflection of the guided wave, 5, under the assumption that the shock layer pressures above and below the jet exhibit limited spatial variation. The expansion subsequently reflects from the lower shear layer as a compression wave, and so on along the supersonic jet. It is assumed that the jet width is sufficiently small that all further reflections of the guided wave remain diffuse. The flow downstream of shock 5 and upstream of the terminating strong shock is therefore isentropic and specification of any one

additional flow property (i.e. the pressure in the surrounding shock layer above or below the jet) is sufficient to determine all remaining flow quantities in this region.

It is remarkable that all the features of the flow discussed above are completely determined, up to an unknown length scale, given only the free-stream conditions and the impinging shock angle. The formation of the supersonic jet and the state of the gas in it are therefore independent of the interaction of the flow with the body. The flow field described above must exist given an incident wave that intersects a sufficiently strong portion of the bow shock ahead of a blunt body. The global flow field about the body must adapt to accommodate the existence of this jet flow structure at some length scale determined by interaction of the local and global flow fields.

1.4. *Jet impingement-point heating model*

Consider next the problem of modelling the heat fluxes at the jet impingement point. In the type IV interaction a portion of the jet passes both above and below the cylinder and so the stagnation streamline must pass through the supersonic jet (figure 1). Whilst stagnation enthalpy is conserved along all streamlines in steady flow, the entropy is lower for streamlines that pass through the relatively weak jet shock system than for streamlines that experience a larger entropy rise across the adjacent strong bow shock waves. Elevated surface pressures are produced at the base of the jet since both pressure and density increase as entropy decreases at constant enthalpy. The elevated density and the strong velocity gradients produced by the impingement of the supersonic jet provide the mechanism for locally increased heat transfer. Edney (1968*a*) used the stagnation-point boundary layer similarity solution of Cohen & Reshotko (1956) to model the heat transfer produced by shock impingement. If one considers the ratio of heating rates with and without shock impingement and invokes the constancy of stagnation enthalpy along all streamlines then the results of Cohen & Reshotko (1956) reduce to a correlation of heat transfer intensification with the pressure (or density) intensification at the impingement point and the ratio of body diameter to jet width, $D/\Delta x$:

$$\left(\frac{\dot{q}_{jet}}{\dot{q}_{body}}\right) \sim \left(\frac{p_{jet}}{p_{body}}\frac{D}{\Delta x}\right)^{1/2}. \tag{1.1}$$

Here the jet heat transfer rate, $\dot{q}_{jet}$, and pressure, p_{jet}, are normalized with respect to the undisturbed stagnation-point values, $\dot{q}_{body}$ and p_{body}.

1.5. *Parametric dependence of the type IV interaction*

To complete the analysis we must link the inviscid model of § 1.3 with the stagnation-point heat transfer model of § 1.4. Specifically we require a prediction of p_{jet} and Δx appearing in equation (1.1). It is possible to predict p_{jet} at the outer edge of the impingement-point boundary layer by assuming that the terminating shock remains normal to the stagnation streamline and given the conditions upstream of the shock. As discussed in § 1.3 it is only possible to bound this state by the pressures existing above and below the supersonic jet. The unknown scale of the impingement flow field, the location of the terminating shock and hence the exact state of the gas upstream of it remain indeterminate. Interaction of the jet with the body determines the unknown length scale. Frame & Lewis (1997) adapt the approximate shock shape methods of Moeckel (1949) to provide a detailed calculation method for the global scales.

Edney (1968*a*) computed the variation of the pressure at the jet impingement point for various free-stream conditions. Figure 3 shows the ratio of jet-impingement

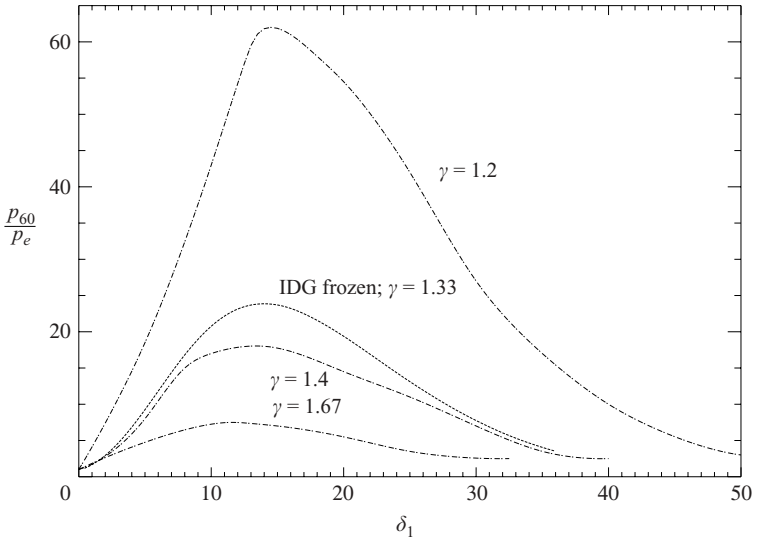

FIGURE 3. Ratio of jet-impingement pressure to undisturbed stagnation-point pressure as a function of incident shock flow deflection angle, δ_1. —·—, The perfect gas model with $M_\infty = 10$ (after Edney 1968*a*, figures 7–9). ····, The current IDG model (refer to § 6 and (6.12)) in the frozen limit with $P_\infty = 0.0075$ and $\alpha_\infty = 0$.

pressure to undisturbed stagnation-point pressure as a function of the flow deflection angle across the incident shock, δ_1, and the ratio of specific heats, γ. The peak pressure initially increases with impinging wave strength before reaching a maximum for moderate strength waves. Significant real gas effects are suggested by the increase in the peak pressure with decreasing ratio of specific heats. The peak pressure also increases strongly with increasing free-stream Mach number. Although the variable-γ model provides only a crude estimate of the influence of equilibrium real gas effects, figure 3 provides strong motivation for further study of the problem in high-enthalpy test facilities.

2. Literature review

Shock interference flow fields are simulated by the provision of an inflow boundary condition ahead of the blunt body that accounts for the discontinuity across the impinging shock. Tannehill, Holst & Rakich (1976) produced one of the earliest attempts at such a simulation; however the results exhibited excessive numerical diffusivity. Although more recent applications of monotonicity-preserving algorithms and unstructured meshing have succeeded in capturing the gross features of the mean flow field, several authors have reported difficulty in obtaining converged numerical solutions for the type IV interaction flow field. Jet oscillations appeared in the computations of Gaitonde (1993) where limit-cycle oscillations were observed in the computational residual as the mesh was adaptively refined. Gaitonde (1993) addressed the issue of time-accuracy of the algorithms that were used and concluded that the oscillations were attributable to the physics of the problem. Similar conclusions may be drawn from the results of Zhong (1994) who also obtained time-accurate solutions for the jet fluctuations using essential non-oscillatory (ENO) schemes. Lind & Lewis (1995, 1996) demonstrate, via detailed time-accurate computations, the potential for

coherent rollup of the shear layers generated at the λ-points coupled with oscillations of the overall jet structure. Edney (1968*a*) commented on oscillations that were observed in the supersonic jet impingement study of Henderson (1966) but did not report any analogous fluctuations of the type IV jet.

Hiers & Loubsky (1967) conducted experiments in a shock tunnel at enthalpies sufficient to produce vibrational excitation and limited oxygen dissociation in air; however the results did not demonstrate any conclusive trends with enthalpy. Wieting & Holden (1989) conducted an experimental study and obtained data detailing the influences of Reynolds number, Mach number and incident shock strength at modest enthalpies. Kortz (1993) and Kortz, McIntyre & Eitelberg (1993) report an experimental investigation conducted at enthalpies sufficient to cause significant nitrogen dissociation in the DLR HEG free-piston shock tunnel. This work included the first quantitative interferometric visualization of shock impingement flows. Elevated heat transfer rates were not observed for the range of parameters that were investigated and this appears to have resulted from a relatively coarse variation of the shock impingement location in the data published to date. The effect of finite-rate chemistry was considered by Hanneman, Brück & Brenner (1993) and Brück (1995) who simulated the experimental results reported by Kortz (1993) and Kortz *et al.* (1993). These computations indicated the persistence of the type IV behaviour for shock-impingement locations intermediate to those discussed by Kortz, and indicated a suppressed reaction rate in the impinging jet fluid. Kinetic theory based simulations of the shock impingement problem that were reported by Carlson & Wilmoth (1994) represent an unusual application of direct simulation Monte Carlo methods. Results were presented for the variation of species concentrations across the shock layer and the impinging jet for a non-catalytic wall that also indicate a suppressed reaction rate in the jet fluid. Borovoy *et al.* (1997) report further data utilizing Mach–Reynolds number scaling along with low-enthalpy data obtained with carbon dioxide test gas and hence $\gamma < 1.4$.

3. Real gas effects

Since the variable-γ model represents only a crude estimate of the influence of flow thermochemistry, a more detailed consideration of the potential influences is warranted. The inviscid reacting flow away from the surface of a hypervelocity vehicle is described by three dimensionless parameters involving the velocity (e.g. Sanderson, Hornung & Sturtevant 2003):

$$M_\infty = \frac{u_\infty}{a_\infty}, \quad H_{0_\infty} = \frac{2mh_{0_\infty}}{k\theta_d}, \quad \Delta_D = \left.\frac{\mathrm{d}\alpha}{\mathrm{d}t}\right|_f \frac{D}{u_\infty}. \tag{3.1}$$

where u_∞ is the velocity of the vehicle, a_∞ is the speed of sound (with frozen chemistry), m is the mass of one atom of the gas (assumed to be diatomic), h_{0_∞} is the total enthalpy, k is Boltzmann's constant, θ_d is a temperature characterizing the energy of the dissociation reaction, $\mathrm{d}\alpha/\mathrm{d}t$ characterizes the reaction rate, the subscript f refers to the chemically frozen state immediately downstream of the bow shock and D is some characteristic dimension of the vehicle. For the case of a vehicle travelling at near orbital speeds the Mach number, M_∞, is large and strong shock waves will be dominant features of the flow. The specific kinetic energy for a vehicle in low Earth orbit at a velocity of $8\,\mathrm{km\,s^{-1}}$ is $32\,\mathrm{MJ\,kg^{-1}}$. Oxygen and nitrogen dissociation occur at specific energies of approximately $k\theta_d/2m = 17\,\mathrm{MJ\,kg^{-1}}$ and $k\theta_d/2m = 34\,\mathrm{MJ\,kg^{-1}}$

respectively and so strong dissociation will occur in the flow about the vehicle. This influence on the equilibrium equation of state is expressed by the dimensionless total enthalpy, H_{0_∞}. The dissociation rate parameter, Δ_D, expresses the finite length over which the reactions occur relative to the size of the vehicle.

The primary effect of dissociation reactions on blunt body flows at large values of the total enthalpy, H_{0_∞}, is to increase the density of the gas in the shock layer. Since shock standoff distances vary inversely with the shock layer density, equilibrium real gas effects must be expected to influence the length scales of the type IV interaction flow field. In the non-equilibrium regime, where $\Delta_D \sim 1$, a thermochemical length scale is introduced into the problem. Variations in the relative magnitudes of the thermochemical and fluid mechanical length scales introduce effects (e.g. Hornung 1972; Hornung & Smith 1979; Wen 1994) that are not encompassed by perfect gas models.

The disparate shock strengths produced at the two mutually inverted λ-points in the type IV flow must be expected to produce strong non-equilibrium effects. Shear layers that are generated at the λ-points cause energy release by mixing the dissociated low-speed fluid with the lower temperature supersonic fluid and this probably influences the shear layer density and spreading rates. This influence of turbulence–chemistry interaction will become important when the type IV jet width is small relative to the shock standoff distance so that turbulent diffusion processes consume the inviscid type IV jet core.

Real gas effects must also be expected to influence the viscous flow in the boundary layer that forms at the impingement point of the inviscid jet core. Recombination occurs in the boundary layer because the wall temperature is low and, in the immediate vicinity of the jet impingement point, the behaviour parallels that of the classical blunt body problem. Fay & Riddell (1958) showed that when the recombination rate in the boundary layer is large,

$$\dot{q} \sim \sqrt{\rho_e \mu_e \left.\frac{\mathrm{d}u_e}{\mathrm{d}x}\right|_0}\, h_0.$$

Here $\dot{q}$ is the heat transfer per unit area and time, and ρ_e, μ_e and $(\mathrm{d}u_e/\mathrm{d}x)|_0$ are the density, viscosity and transverse velocity gradient respectively at the outer edge of the boundary layer. Jet impingement does not influence the total enthalpy at the stagnation point, h_0, since stagnation enthalpy is conserved at all points in steady flow. This also implies a limited influence on the viscosity, μ_e, since for diatomic gases $\mu_e \sim T_e^{0.7} \sim h_0^{0.7}$. The most important real gas influences on the impingement point flow are therefore the increased density of the outer flow, ρ_e, and the coupled effect on the velocity gradient. Continuity implicitly couples the density and velocity gradient at the edge of the boundary layer. Finally, note that shock impingement greatly increases the recombination rates in the boundary layer since these scale with the square of the density at the jet impingement point.

We conclude that both equilibrium and finite-rate real gas effects may be expected to exert a significant influence on the type IV interaction flow field. A broad range of possible influences arise as a consequence of the strong interdependence of real gas effects and the elevated densities produced by shock impingement. Despite the magnitude of the real gas effects predicted by Edney (1968*a*) and the severity of the phenomenon, systematic experimental or parametric numerical studies have yet to appear.

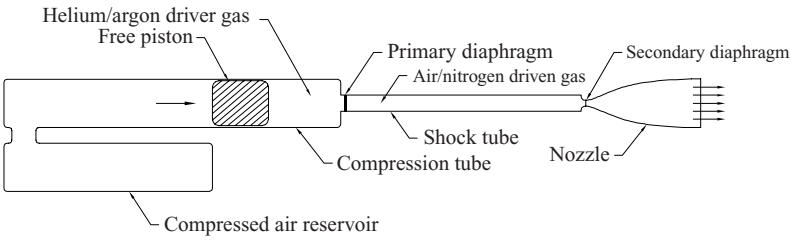

FIGURE 4. Schematic arrangement of T5 free-piston hypervelocity shock tunnel.

4. Description of experiment

4.1. *Free-piston shock tunnel*

The current work consists primarily of an experimental investigation of the shock interaction problem that utilizes the capabilities the GALCIT T5 hypervelocity shock tunnel to determine the quantitative effects of flow thermochemistry. Based on these experimental observations, we aim to develop models of the important mechanisms and provide quantitative predictions of the influences of the controlling parameters. Equations (3.1) express the requirements for similitude in a hypervelocity ground testing facility. The development of free-piston driver shock tunnels, by Stalker (1967) and coworkers, has enabled the simulation of these dimensionless parameters in the laboratory – i.e. the production of a high-stagnation-enthalpy test flow at sufficiently high density to scale the non-equilibrium kinetics of the flow about vehicle surfaces. The T5 facility is illustrated schematically in figure 4 and further details of the performance and construction of this complex facility are given by Hornung *et al.* (1991). In order to achieve a sufficiently high shock speed at high density, the speed of sound of the driver gas is raised by adiabatically compressing the driver gas with a single stroke of a reusable compressed-air-driven piston. A strong primary shock wave was generated by the pressure and temperature difference across the diaphragm at burst. A secondary shock wave was reflected from the nozzle throat, recompressing and reheating the test gas before crossing the test gas–driver gas interface and propagating back along the length of the shock tube. The resulting reservoir of dissociated test gas was expanded through a converging–diverging nozzle into the evacuated test section. Three different test conditions were used and these are summarized in table 1. The Mach number and Reynolds number of the flow decreased as the stagnation enthalpy was increased and this complicates interpretation of the current results. Coupling of these parameters in the data with a single nozzle area ratio was unavoidable.

At sufficiently long test times the test flow becomes contaminated with the helium–argon driver gas mixture (Davies & Wilson 1969) and this contamination is accelerated by high-enthalpy test conditions that decrease the specific volume of the test gas, thereby moving the driver–test gas interface closer to the nozzle throat. Progress is evident in the literature for direct determination of the contamination free test time (Paull 1996; Sudani & Hornung 1998) and in techniques for delaying the onset of driver gas contamination (Sudani, Valiferdowsi & Hornung 2000). The holographic interferograms obtained in the current experiment were exposed at $t = 2.125$ ms, 1.625 ms and 1.275 ms after primary shock reflection for test conditions A, B and C respectively. The data of Sudani *et al.* (2000) (including consideration of the effect of driver/test gas interface tailoring) indicate the onset of contamination, based on a $6.5 \pm 1.5\%$ by volume threshold, at $t > 3$ ms, 2.3 ms and 1.7 ms after primary shock reflection for test conditions A, B and C respectively.

Test condition		A	B	C
Shock tube conditions	Fill pressure (kPa $\pm$ 0.5 kPa)	75	32.5	20
	Fill temperature (K $\pm$ 4 K)	297	297	297
	Shock speed ($m\,s^{-1}$)	1890 $\pm$100	3500 $\pm$245	4360 $\pm$255
Nozzle reservoir conditions	Pressure (MPa)	14.6 $\pm$0.7	22.3 $\pm$1.3	28.3 $\pm$1.9
	Temperature (K)	3210	7550	8960
	Enthalpy ($MJ\,kg^{-1}$)	3.88	12.0	19.1
Test section conditions	Velocity ($m\,s^{-1}$)	2540	4450	5350
	Density ($kg\,m^{-3}$)	0.0218	0.0155	0.0157
	Pressure (kPa)	1.03	5.48	11.4
	N concentration ($mole\,kg^{-1}$)	9.9×10^{-5}	6.9×10^{-1}	3.65×10^{0}
Test section dimensionless parameters	IDG P_∞	7.32×10^{-3}	1.79×10^{-2}	2.54×10^{-2}
	IDG H_{0_∞}	0.102	0.346	0.560
	IDG α_∞	1.4×10^{-6}	9.7×10^{-3}	0.051
	IDG $\hat{\rho}_d$	6.0×10^{6}	8.4×10^{6}	8.3×10^{6}
	IDG Δ (mm^{-1})	$4. \times 10^{-13}$	3.4×10^{-2}	0.525
	Re (mm^{-1})	5540	1630	1350
	Re_D	222000	65200	54000
	M_∞ (assuming $\gamma = 4/3$)	9.9	6.3	5.3
	$\hat{\rho}_e$	6.61	8.59	9.67
	α_e	2.0×10^{-6}	0.114	0.285
	St	0.0123	0.0172	0.0167
	$\beta_1(\pm 1^\circ)$	14.25	15.0	16.0

TABLE 1. Summary of the free-stream conditions. Test conditions were computed (Sanderson 1995) on the basis of measurements of the initial shock tube fill pressure and temperature, incident shock speed prior to reflection, and nozzle reservoir pressure after shock reflection. The dimensionless parameters for the ideal dissociating gas (IDG) model are defined in § 6.2. Error estimates given for the fill conditions represent the accuracy of the pressure gauge and the variation of the ambient temperature. Error estimates for the measured shock speed and reservoir pressure are the standard deviation of the quantities sampled over the entire sequence of shots. The error in the computed quantities may be inferred from these estimates.

4.2. *Test section arrangement*

The experimental arrangement is shown in figure 5. The gas was expanded into the test section using a contoured axisymmetric nozzle with an area ratio of 109 and an exit diameter of 315 mm. A cylinder with aspect ratio 4.5 provided the largest model that adequately approximated a two-dimensional flow (based on the data of Sykes 1962) and optimization of the geometrical arrangement led to a model diameter of 40.6 mm. The surface temperature rise of the model during the test time was sufficiently small to approximate an isothermal wall boundary condition. Section 6.4 shows that recombination rates in the model boundary layer are sufficiently large that recombination occurs irrespective of the degree of catalysis provided by the model surface. Since the surface temperature remains low the boundary condition $\alpha = 0$ applies. A large shovel-shaped shock generator was partially inserted into the uniform nozzle core flow that extends upstream of the nozzle exit plane. Shock generators of this type produce a planar oblique shock wave, with uniform downstream flow, and are closely related to a class of supersonic lifting body shapes known as wave-riders (Nonweiler 1959). Variations in the shock impingement flow field were produced by

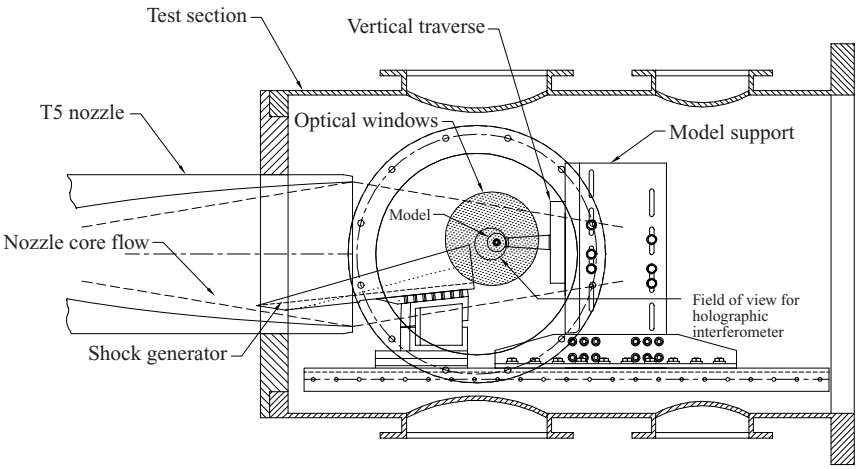

FIGURE 5. Layout of apparatus in the test section of T5 (to scale).

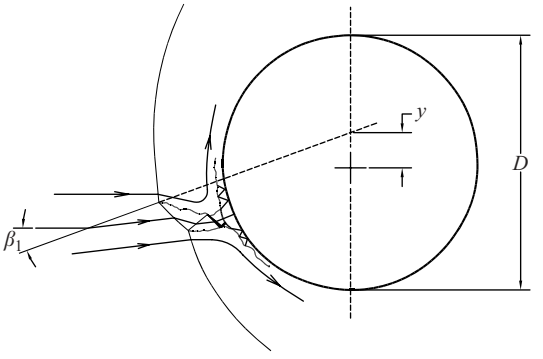

FIGURE 6. Specification of interaction geometry in terms of incident shock angle, β_1, and incident shock location relative to body, y/D.

vertically translating the model with respect to the exit of the shock generator. The shock generator was inclined at an angle of 6° for all experiments described in the current paper. This shock generator configuration efficiently utilizes the available test section space, allows considerably larger models to be tested, and thereby enhances the reaction scaling capability of the test facility. Since the flow in the nozzle is predicted to exhibit some angularity and Mach number non-uniformity at the low-enthalpy off-design conditions A and B, the actual shock angles lay slightly further from the surface of the wedge than indicated by simple calculation. The measured shock angles that form the best basis for data analysis are listed in table 1. The geometry of the interaction is completely determined by the specification of one additional dimension giving the vertical position of the impinging shock relative to the body (see figure 6). Sanderson (1995) gives holographic interferograms and heat transfer data for a range of impinging shock locations. The interferograms shown here are a subset that best illustrate the circumstance whereby the stagnation streamline coincides with the centreline of the supersonic jet. In computational simulations, the location of the

Wavelength	$\lambda = 532\,\text{nm}$
Path length	$L = 0.180\,\text{m}$
Gladstone–Dale constants	$K_N = 3.1 \times 10^{-4}\,\text{m}^3\,\text{kg}^{-1}$
	$K_{N_2} = 2.45 \times 10^{-4}\,\text{m}^3\,\text{kg}^{-1}$

TABLE 2. Physical constants for holographic interferograms. The fringe shift observed in the interferograms is given by $\theta/2\pi = (\rho - \rho_\infty)[K_{N_2}(1-\alpha) + K_N\alpha]L/\lambda$, where θ is the phase shift relative to the free stream, ρ is the density, ρ_∞ is the density of the free stream and α is the dissociation fraction.

impinging shock wave should be similarly adjusted to achieve a flow topology whereby the stagnation streamline coincides with the midpoint of the jet.

4.3. *Instrumentation*

Sensors were available to monitor the operating parameters of the shock tunnel prior to release of the free piston and the subsequent initiation of the shock wave. Piezo ceramic pressure transducers were installed along the length of the shock tube to assist in the determination of the free-stream conditions. Passage of the incident and reflected shock waves past the transducers allowed calculation of shock speeds. One of these pressure transducers, installed in the downstream end of the shock tube, served the additional purpose of measuring the nozzle reservoir pressure.

Surface junction thermocouples were used to record the time-resolved surface temperature at 24 circumferential locations around the model forebody. The sensitive area of the gauges subtended an angle of 2° at the centre of the cylinder and were spaced at 5° intervals in the most densely instrumented portion. Surface heat fluxes may be inferred from the time histories of the surface temperatures via a semi-infinite body model of transient heat conduction into the model. Sanderson & Sturtevant (2002) describe the mean-square optimal spectral method that was used to solve the resulting inverse problem along with the gauge design that was used to ensure adequate high-frequency response. The heat transfer measurements are subject to lateral conduction errors when the heat transfer rates are highly localized. The relevant thermal diffusion length scale here is $(\alpha t)^{1/2} \sim 0.1\,\text{mm}$ and this is subordinate to the spatial resolution of the transducers (0.8 mm).

The instantaneous heat transfer distribution was plotted for each interferogram along with an average value taken over an interval of width 100 μs (e.g. figure 7). The instantaneous profile and the centre of the averaging interval correspond to the time at which the hologram was recorded. Superimposed on these plots are the standard deviations of the time histories over the averaging interval. This gives an indication of the temporal fluctuations of the heat transfer rates at various locations on the model surface. The final set of points on each plot is the envelope of the maximum heat transfer rate recorded at each circumferential location during the shot.

A $\phi 75\,\text{mm}$ field of view holographic interferometer was constructed and used to visualize the flow field and to provide quantitative measurements of the density field (see table 2). The fundamentals of the technique and the interpretation of the resulting interferograms are described in the literature (e.g. Merzkirch 1974). The interferogram produced is equivalent to an infinite-fringe Mach–Zehnder interferogram, averaged along the line of sight through the test section. Further details of the design and construction that are unique to high-enthalpy shock tunnels are given by Sanderson (1995).

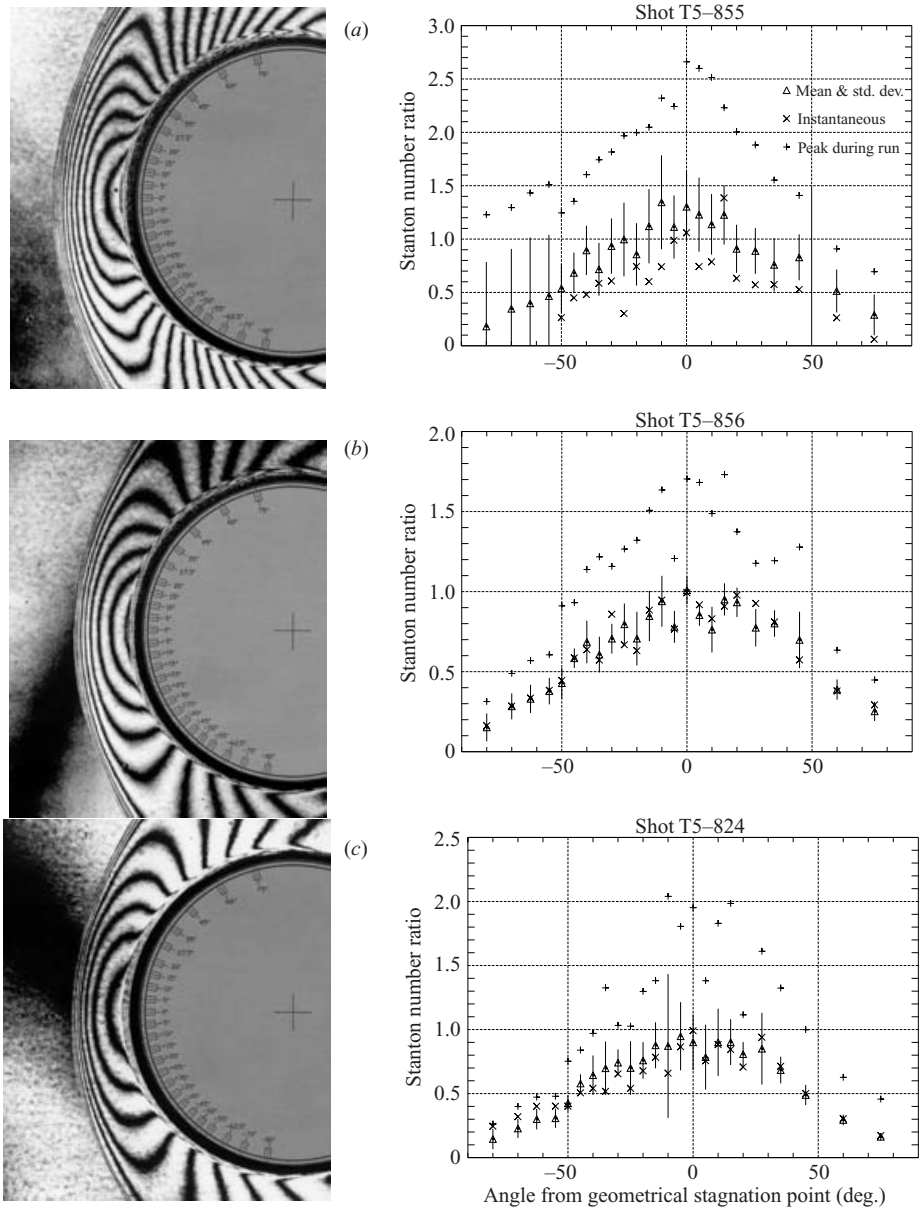

FIGURE 7. Holographic interferograms and Stanton number ratio, $St/St_{Fay\&Riddell}$ for flows without shock wave impingement. Test conditions are (*a*) A, (*b*) B and (*c*) C (see table 1).

5. Experimental results

5.1. *Flows without shock impingement*

The flow about the cylinder without shock wave impingement is shown for each of the three test conditions in figure 7. The heat transfer data have been reduced to Stanton number form and normalized with respect to the predicted stagnation-point heat transfer rate due to Fay & Riddell (1958). The small wall enthalpy has been

Test condition	A	B	C
Undisturbed fringe shift	13 ± 1	10.5 ± 1	9 ± 1
Type IV fringe shift	55 ± 2	29.5 ± 1	27 ± 1
Ratio	4.2 ± 0.5	2.81 ± 0.4	3.0 ± 0.4

TABLE 3. Stagnation-point fringe shift for type IV flows with cylindrical model.

neglected in the definition of the Stanton number for hypervelocity flow,

$$St = \frac{\dot{q}}{\rho_\infty u_\infty h_{0_\infty}}. \tag{5.1}$$

The heat transfer model is detailed in §§6.4 and 6.5 and numerical values for the predicted stagnation-point Stanton number without shock impingement at each test condition are given in table 1. Sanderson & Sturtevant (2002) show formally that the heat transfer data and predictions without shock impingement agree within experimental uncertainty.

5.2. *Type IV flows*

When the shock impinges in the vicinity of the geometrical stagnation point the high-heating-rate type IV configuration occurs. The stagnation-point fringe shifts in figure 8 at low, medium, and high enthalpy respectively may be measured from enlargements of the interferograms and compared with the values without shock impingement (table 3). Although these measurements indicate a trend towards reduced density intensification at high enthalpy, care must be taken in comparison of these highly localized measurements that are sensitive to variations across the span of the model. Spanwise non-uniformity is evident in the multiple images of shock fronts that are observed along the line of sight in the interferograms. The non-uniformity is ascribed to slight out-of-plane curvature of the incident shock wave, the strong sensitivity of the flow field to impingement location, and potential unsteady oscillations of the jet structure that are not synchronous along the span of the cylinder. Comparison of the type IV thermocouple data shown in figure 8 indicates a similar trend of reduced heat transfer intensification at the higher enthalpy conditions, and importantly these data are insensitive to variations across the span of the model. In all cases the maxima of fringe shift and instantaneous heat transfer occur at the same angular location. The standard deviation of the heat transfer data increases in the vicinity of the jet impingement point, indicative of flow unsteadiness.

5.3. *Unsteadiness of the type IV jet structure*

The instrumentation and signal processing techniques that are described by Sanderson & Sturtevant (2002) provided unusually high bandwith measurements of the heat transfer intensification caused by shock impingement. These measurements reveal further details of the fluctuations of the type IV jet flow that are discussed in the literature (see §2). Evidence for coherent unsteadiness is also observed in the interferograms of figure 8. Unsteady structures appear to be generated at the jet impingement point and convect along the surface of the body. Figure 9 demonstrates the time history of the surface heat flux in the vicinity of the type IV jet impingement point for test condition A as shown in figure 8. The frequency spectrum obtained using standard FFT methods for the thermocouple gauge at $\theta = -25^\circ$ indicated only

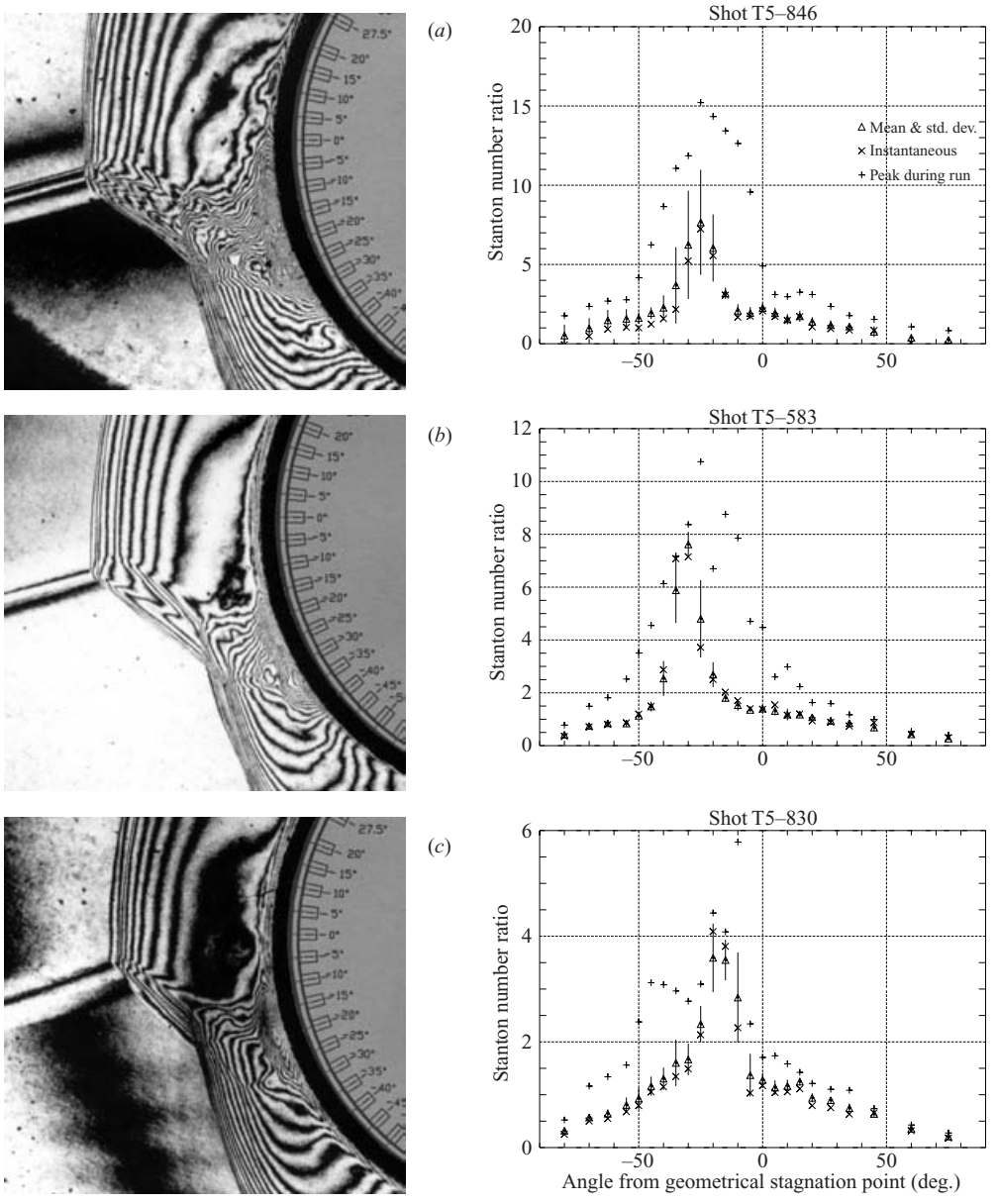

FIGURE 8. Holographic interferograms and heat transfer distributions for type IV interactions at conditions (*a*) A, (*b*) B and (*c*) C. Details of the test conditions are given in table 1. The geometry of the interaction is defined by condition A: $\beta_1 = 14.8°$, $y/D = 0.156$; condition B: $\beta_1 = 15.8°$, $y/D = 0.131$; condition C: $\beta_1 = 18.0°$, $y/D = 0.194$; (refer to § 4.2 and figure 6).

a weakly defined local maximum of the heat flux power spectral density at 6.5 kHz. Each fluctuation of the oscillation cycle is observable in figure 9 as a spike in the heat transfer rate and a sawtooth-shaped perturbation of the surface temperature record. This characteristic sawtooth shape reflects the response of the gauge substrate to an impulsively applied thermal load (see Sanderson & Sturtevant 2002) caused by the passage of the oscillating jet past the heat transfer gauge location.

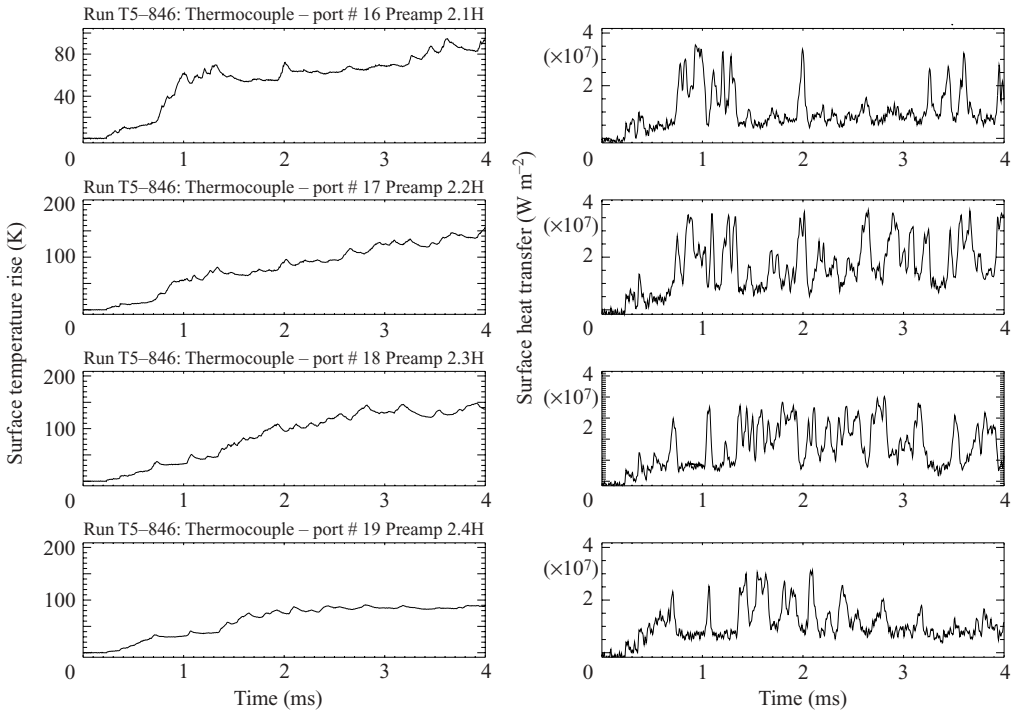

FIGURE 9. Temporal variation of the surface heat flux for type IV flow at condition A; Shot T5-846. Top to bottom: $\theta = -15°$, $-20°$,$-25°$, $-30°$.

Robust estimates of a Strouhal number for the data of figure 9 were obtained through application of elementary graphical cycle counting methods to the heat transfer time records (refer to Collins (1981) for a discussion of cycle counting methods, in the context of fracture mechanics). Figure 10 indicates a threshold crossing rate of 18 kHz at the jet impingement location, corresponding to a cyclic fluctuation of the heat transfer rate of 9 kHz (since both positive and negative going threshold crossings are considered) and to an underlying 4.5 kHz oscillation of the flow structure since the jet sweeps twice across the impingement location during each cycle (upwards and downwards). Note however that at the end points of the sweep of the impinging jet, away from the peak heating location, only one peak in the heat transfer rate is expected per cycle of the jet. This conclusion is supported by the approximately halved threshold crossing rates observed in figure 10 above ($-20°$: 9.1 kHz) and below ($-30°$: 8.8 kHz) the peak heating location ($-25°$: 18.0 kHz). The heat transfer rate at the mean impingement location ($\theta = -25°$) in figure 9 fluctuates between well-defined lower ($\approx 0.5 \times 10^7$ W m^{-2}) and upper bounds ($\approx 3.5 \times 10^7$ W m^{-2}) and the instantaneous heat transfer rate is uniformly distributed between these upper and lower bounds over the time interval of interest ($1.125 \rightarrow 3.125$ ms). Away from the peak heat transfer location ($\theta = -20°$, $\theta = -30°$) however, the distribution is biased towards the lower bound. This is consistent with a jet that sweeps only briefly, at the end of its travel, across the heat transfer gauges away from the mean jet impingement location.

Using the free-stream data from table 1, the frequency of oscillation for condition A may be expressed as a diameter-based Strouhal number, $Sh_D = f D/u_\infty \approx 0.072$. Oscillations were observed in the time-resolved computations of Gaitonde (1993)

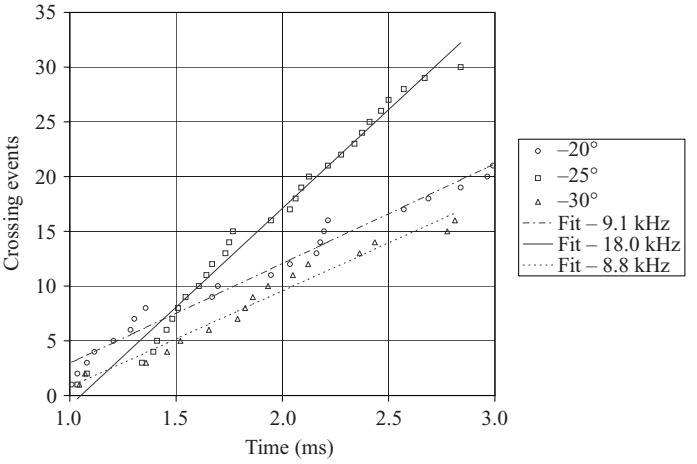

FIGURE 10. Heat transfer threshold crossing events for Shot T5-846 at test condition A for gauges situated at $-20°$, $-25°$, $-30°$. A window of heat transfer data was selected, spanning ± 1 ms about the laser firing time, and the minimum and maximum heat transfer rates observed during this window were noted. A threshold heat transfer level was then selected midway between the minimum and maximum levels. Positive and negative going crossings of this threshold level were then determined and plotted.

and Zhong (1994) who simulated the experimental results of Wieting & Holden (1989). Both computations independently predicted the result $Sh_D \approx 0.65$. It should be noted that convergence of the oscillation cycle was not achieved. Grid refinement produced continually increasing modulation of the fluctuation cycle and this was much less than that shown in figure 9. Gaitonde (1993) cites additional experiments by Holden that indicated a Strouhal number in the range $Sh_D = 0.065$–0.22. This agrees tolerably well with the current data at condition A. In all cases we assume that the data are reported at the peak heating location, and so halve the reported frequency of the heat transfer or pressure fluctuations, to report a diameter-based Strouhal number for the underlying jet motion.

Peak heating was fortunately achieved for only a short period of time at the higher enthalpy test conditions, B and C. This occurred because the shock generator was long with respect to the diameter of the model so that small variations in the shock angle during the test time produced a larger effect on the position of the impinging wave. The type IV configuration is strongly sensitive to the impinging shock location. Although the time histories of the heat transfer rates were qualitatively the same as discussed for test condition A, the quality of frequency spectra of the surface heat flux at conditions B and C were severely limited by the small number of cycles that were observed, and no reliable estimates of Strouhal numbers were possible.

5.4. *Summary of the experimental data*

Figure 11 summarizes the heat transfer data at test conditions A, B and C respectively. Each plot represents a compilation of the heat transfer data over a sequence of shots at each test condition. The first set of points, $+$, is the maximum instantaneous heat flux recorded at each circumferential location on the model. The maximum is determined over all shots at the same test condition and is assessed throughout a time interval that excludes flow starting transients and extends over the period of useful test time. The second set of points, $\triangle$, results from the same maximization

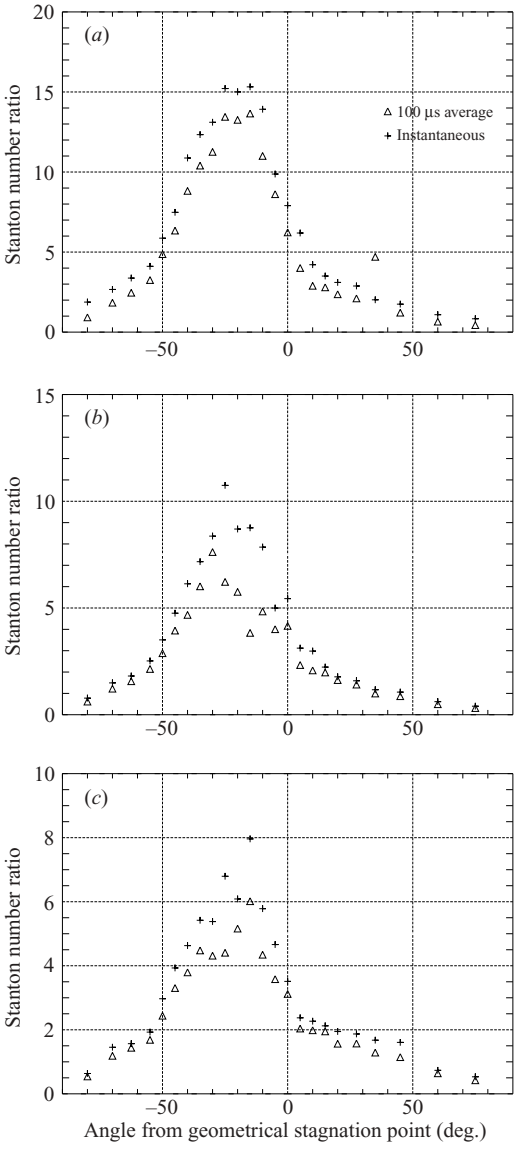

FIGURE 11. Envelope of maximum heat transfer rates around the model at conditions (*a*) A, (*b*) B and (*c*) C (see table 1). The anomalous point at $\theta = 35°$ for condition A arises from contributions to the average beyond the ends of the sampling period.

procedure; however the data were first averaged over an interval of 100 μs. This peak and averaged data format corresponds to that used to report heat transfer data for each of the individual interferograms. We conclude from these statistics that both the peak and averaged heat transfer intensification decreased by a factor of two as the stagnation enthalpy was increased from $H_{0_\infty} = 0.10$ to $H_{0_\infty} = 0.56$ simultaneously with a decrease in the Mach number from $M_\infty = 9.9$ to $M_\infty = 5.3$ at test conditions A and C respectively (see table 1 for additional variations in the remaining parameters). In addition to the multiple parameter variations involved, care must be taken in the interpretation of this trend since the data have been reduced to dimensionless

Reference	M_∞	δ_1 (deg.)	H_{0_∞}	Δ_D	Re_D	Geometry	Gas	$\hat{q}$
Edney (1968*a*)	4.6	5	0.019	0	4.3×10^5	Sphere	Air	6.5
	4.6	10	0.019	0	4.3×10^5	Sphere	Air	7.5
	4.6	15	0.019	0	4.3×10^5	Sphere	Air	10
	7.0	5	0.019	0	1.6×10^5	Sphere	Air	8
Wieting & Holden (1989)	8.0	10	0.048	0	3.9×10^5	Cylinder	Air	13
	8.0	12.5	0.048	0	3.9×10^5	Cylinder	Air	18
	8.0	15	0.048	0	3.9×10^5	Cylinder	Air	25
	6.3	10	0.036	0	1.2×10^6	Cylinder	Air	11.5
Figure 11	9.9	9.8	0.102	6.3×10^{-11}	2.2×10^5	Cylinder	N_2	13.5
	6.3	7.7	0.346	2.2	6.5×10^4	Cylinder	N_2	7.5
	5.3	6.9	0.560	50.3	5.4×10^4	Cylinder	N_2	6

TABLE 4. Comparison of measured heating rates from previous studies.

form – the dimensional heat transfer rate increases considerably with stagnation enthalpy.

5.5. *Comparison with existing data*

In order to achieve a reliable comparison of the current data with existing results we must consider the influence of the multiple parameters involved. Differences in the free-stream conditions, model geometry and extent of real gas effects must be considered. Table 4 lists the peak heating rates observed by various authors including the benchmark data of Edney (1968*a*), the extensive Mach–Reynolds number scaling experiments of Wieting & Holden (1989) and the current non-equilibrium binary scaling data. In choosing a valid data set for comparison we must consider the differing instrumentation and tunnel operating conditions used by the various authors. Specifically we include only data that were obtained using fast response surface sensors able to resolve the temporally fluctuating peak heat transfer rate (Edney 1968*a*; Wieting & Holden 1989 – Calspan hypersonic shock tunnel only) and exclude data obtained using calorimetric heat transfer sensors (Borovoy *et al.* 1997; Wieting & Holden 1989 – NASA high-temperature tunnel). Further we exclude the initial high-enthalpy data obtained by Kortz (1993) (see also Kortz *et al.* 1993) over a modest range of impingement locations and the carbon dioxide data of Borovoy *et al.* (1997) that scale non-equilibrium effects in the sense of Edney (with $\gamma < 1.4$) but do not lie in the non-equilibrium regime. Differing spatial and temporal resolution of the instrumentation that was used by the various authors complicates this comparison and the use of 100 μs time-averaged values from the current study represents the best compromise. Data obtained with calorimetric sensors must be considered separately.

Generally, we expect the following dimensionless dependence of the heat transfer intensification, $\hat{q}$:

$$\hat{q} = f\left(M_\infty, \delta_1, H_{0_\infty}, \Delta_D, Re_D, \Gamma, \hat{\rho}_d, \alpha_\infty\right), \tag{5.2}$$

where M_∞ is the free-stream Mach number, δ_1 is the flow deflection angle across the incident shock wave, H_{0_∞} is the free-stream total enthalpy normalized with respect to the dissociation energy of the gas, Δ_D is the reaction rate parameter, Re_D is the Reynolds number based on diameter, Γ is a set of parameters describing the geometry, $\hat{\rho}_d$ is a dimensionless equilibrium parameter, and α_∞ is the free-stream dissociation level. Since H_{0_∞} and Δ_D are not varied independently in the current experiments, we choose to consider only H_{0_∞}. Further we neglect $\hat{\rho}_d$ and α_∞ since these are reasonably

assumed to be secondary parameters. We therefore expect the experimental data to be regressed by

$$\hat{q} = f\left(M_\infty, \delta_1, H_{0_\infty}, Re_D, \Gamma\right). \tag{5.3}$$

Further, based on the predictions of Edney's model for a given gas, in the absence of effects due to gas dissociation and turbulent diffusion in the impinging jet, we expect

$$\hat{q} = f(M_\infty, \delta_1, \Gamma). \tag{5.4}$$

Note that here the local interaction effects are determined by the parameters M_∞ and δ_1 whereas the influence of the global length scales is captured by the set of geometric parameters, Γ. Based on the form of the solution of Edney's model in the weak impinging wave region, away from the local maximum that occurs (see figure 3), we propose the following multiplicative form for the relationship between the parameters (excluding geometry):

$$(\hat{q} - 1) \approx \phi_0 (M_\infty - 1)^{\phi_1} \delta_1^{\phi_2}, \tag{5.5}$$

with the choice of terms $(\hat{q} - 1)$ and $(M_\infty - 1)$ being motivated by the expected behaviour in the limits $\delta_1 \to 0$ and $M_\infty \to 1$. Here ϕ_1, ϕ_2 and ϕ_3 are unknown dimensionless constants. Flow deflection angle, δ_1, is chosen as a regression variable in preference to the shock angle, β_1, since the limit $\delta_1 \to 0$ is convenient. Proceeding by the usual method of logarithmic transformation and method of least squares for the unknown parameters we obtain

$$(\hat{q} - 1) \approx 9.0 (M_\infty - 1)^{0.88} \delta_1^{0.78}, \tag{5.6}$$

with an 85% correlation coefficient and with all three parameters determined to >99.5% level of statistical significance.

It remains to consider the role of the remaining parameters $(H_{0_\infty}, Re_D, \Gamma)$ in explaining the residual 15% variability in the observed heat transfer intensification. Proceeding by the usual two-sample Student's t-test for the residuals of the previous regression, geometry Γ is rejected as a viable parameter at <50% statistical significance. This reinforces the observation that the type IV interaction is indeed driven by local effects at the impingement point. Regression for the full set of parameters (excluding geometry) in equation (5.3) takes the form

$$\hat{q} - 1 \approx \phi_0 (M_\infty - 1)^{\phi_1} \delta_1^{\phi_2} H_{0_\infty}^{\phi_3} Re_D^{\phi_4}. \tag{5.7}$$

Only unreliable estimates of ϕ_3 and ϕ_4 are obtained at <50% statistical significance and so no meaningful dependence of the data on H_{0_∞} and Re_D is discernible. Clearly this is contrary to the expectation (refer § 1.5) of greatly increased heat transfer intensification at high enthalpy and the regression analysis represents a formal assessment of the conclusions that may be drawn directly from the experimental work. The heat transfer enhancement is plotted against the regression equation (5.6) in figure 12.

6. Model of the influence of non-equilibrium thermochemistry

6.1. *Introduction*

Recall that in § 1.2 we considered the structure of the type IV flow field to be composed of an inviscid jet shock system with the eventual heat transfer rate being determined by the impingement of the jet onto the surface of the body. In order to reconcile the current experimental data with the existing belief of a strong influence of real gas effects, we must improve the prior variable-γ model that provides only a crude estimate of the influence of equilibrium real gas effects. We seek a model that

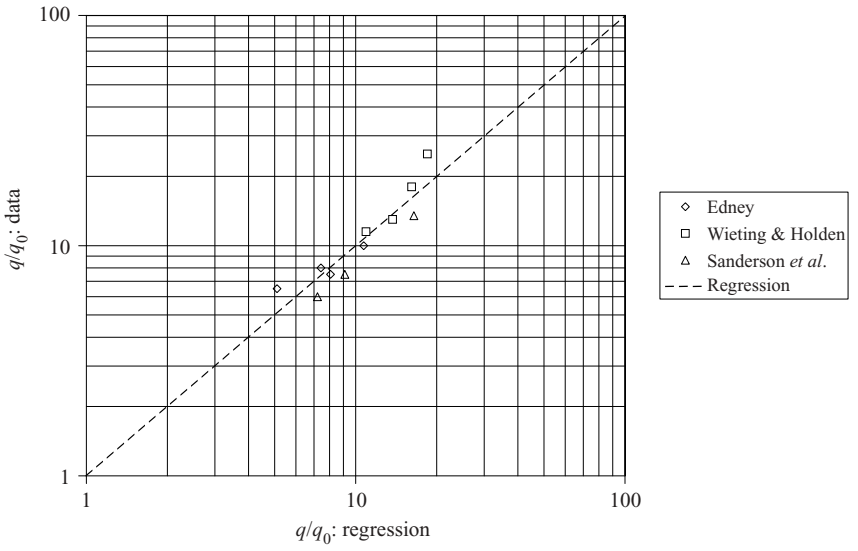

FIGURE 12. Comparison of heat transfer data against prior studies. The heat transfer intensification, $\hat{q}$, is plotted as a function of the regression equation (5.6). The experimental data and test conditions are given in table 4.

illustrates the important thermochemical mechanisms occurring in both the inviscid jet and at the impingement point.

The current data also reveal the important role of unsteadiness in the type IV interaction. Neither existing models nor the current model encompass this aspect of the problem. In what follows we assume that the jet structure sweeps slowly across the body, relative to the fluid mechanical time scales in the jet and boundary layer. The results given therefore predict the peak instantaneous heating rate experienced during the oscillation of the jet over the surface of the body. Modelling and correlation of important parameters including the frequency and amplitude of the oscillation lie beyond the scope of the current experiments and analysis. From an engineering standpoint these parameters are critical in determining the structural response and the spatial mollification of the intense heat loading over a region of the body surface. Note that the mechanisms driving the oscillation may be significantly modified in fully three-dimensional interactions such as those that occur between an oblique shock wave and a spherical body, and between an oblique shock wave and a blunted fin.

6.2. *Shock wave model*

We first extend the methodology for mapping the flow field in the vicinity of the shock wave intersection points into the pressure–flow deflection angle (p, δ)-plane. This methodology has been developed in a separate paper by the authors (Sanderson *et al.* 2003) who present a compact dimensionless framework for the analysis of normal, oblique and interacting shock waves. The thermochemical models used are due to Lighthill (1957) and Freeman (1958) concerning the relaxation to equilibrium of the system

$$\mathrm{N_2 + M \rightleftharpoons N + N + M} \tag{6.1}$$

where nitrogen is the prototypical gas and M represents a non-reacting third body. The shock structure considered here neglects the translational and rotational shock thickness and resolves only the relaxation of the internal modes over a length scale

comparable to that of the fluid motion. Consider initially a one-dimensional normal shock wave. The following parameters arise:

$$P_1 = \frac{p_1}{\rho_1 u_1^2}, \tag{6.2}$$

$$\Theta_1 = \frac{\theta_d}{T_1}, \tag{6.3}$$

$$K_1 = \frac{m u_1^2}{k\theta_d}, \tag{6.4}$$

$$H_{0_1} = \frac{2mh_{0_1}}{k\theta_d}, \tag{6.5}$$

$$\alpha = \frac{n_N}{n_N + 2n_{N_2}}. \tag{6.6}$$

Here ρ is the density of the gas, u is the velocity normal to the shock, p is the pressure and h_0 is the total enthalpy per unit mass, k is Boltzmann's constant, m is the mass of one atom of the gas, T is the temperature, θ_d is a temperature characterizing the dissociation energy and α is the dissociated mass fraction determined from the number densities, n_N and n_{N_2}. The subscripts, 1 and 2, refer (contrary to prior use in the context of figure 1) to the upstream and downstream states respectively and generally the notation $\hat{\phi} = \phi_2/\phi_1$ applies. Note that P_1 behaves as $P_1 \sim 1/M_1^2$ for a perfect gas. The conserved stagnation enthalpy, H_{0_1}, is normalized with respect to the dissociation energy of the gas and K_1 is the normalized specific kinetic energy of the upstream flow. Three parameters are sufficient to define the state of the upstream gas and here we specify P_1, H_{0_1} and α_1 (Sanderson *et al.* 2003 give identities for the remaining dependent parameters). Proceeding by application of the conservation equations across the translational and rotational discontinuity and invoking the caloric and thermal equations of state for an ideal dissociating gas, we obtain the following result that applies throughout the relaxation region downstream of a normal shock:

$$(H_{0_1} - \alpha_2)\hat{\rho}^2 - 2K_1(1 + P_1)\frac{4 + \alpha_2}{1 + \alpha_2}\hat{\rho} + K_1\frac{7 + \alpha_2}{1 + \alpha_2} = 0. \tag{6.7}$$

(Note that this expression is valid for $\alpha_1 \neq 0$, as required for shock wave interaction problems, since the dependence is captured in $K_1 = K_1(P_1, H_{0_1}, \alpha_1)$). In the chemically frozen limit, $\alpha_2 = \alpha_1$, equation (6.7) has solutions

$$\hat{\rho}_f = \begin{cases} 1, \\ \dfrac{7 + \alpha_1}{(1 + \alpha_1) + 2P_1(4 + \alpha_1),} \end{cases} \tag{6.8}$$

and in the equilibrium limit far downstream of the shock we have

$$\frac{\alpha_{2_{eq}}^2}{1 - \alpha_{2_{eq}}} = \frac{\hat{\rho}_{d_1}}{\hat{\rho}_{eq}} \exp\left(\frac{\left(1 + \alpha_{2_{eq}}\right)\hat{\rho}_{eq}^2}{2K_1(1 - \hat{\rho}_{eq}(1 + P_1))}\right). \tag{6.9}$$

An additional dimensionless equilibrium constant is introduced,

$$\hat{\rho}_{d_1} = \rho_d/\rho_1. \tag{6.10}$$

The dissociation reaction proceeds from the frozen state to the equilibrium state at rate

$$\frac{\mathrm{d}\alpha_2}{\mathrm{d}\hat{x}} = \ell_{d_1}\frac{\mathrm{d}\alpha_2}{\mathrm{d}x} = \hat{\rho}^2\hat{T}^\eta\Theta_1^{-\eta}\left[(1 - \alpha_2)\exp\left(-\Theta_1/\hat{T}\right) - \frac{\hat{\rho}}{\hat{\rho}_{d_1}}\alpha_2^2\right], \tag{6.11}$$

with

$$\frac{\Theta_1}{\hat{T}} = \frac{\hat{\rho}^2(1+\alpha_2)}{2K_1(\hat{\rho}(P_1+1)-1)}. \tag{6.12}$$

Here C is the reaction rate constant, η represents the pre-exponential temperature dependence of the reaction rate and $\ell_{d_1} = u_1/(C\rho_1\theta_d^\eta)$ is the characteristic reaction length. The above results are sufficient to elucidate the discussion that follows.

6.3. *Reacting-flow jet shock solution*

The extension to oblique waves, the provision of jump relations for all parameters across the shock, the consistent normalization of the reaction rates and the mapping into the (p, δ)-plane as required for analysis of multiple shock wave interactions are developed by Sanderson *et al.* (2003) who adopt the notation

$$\left(\hat{\rho}_2, \hat{p}_2, \delta_2, P_2, H_{0_2}, \alpha_2\right) = \mathscr{J}\left(P_1, H_{0_1}, \alpha_1, \hat{\rho}_d, \beta_1\right). \tag{6.13}$$

Applying this notation to the idealized flow field for the Edney type IV interaction (figure 1) we obtain the system of equations

$$(\hat{\rho}_2, \hat{p}_2, \delta_2, P_2, H_{0_2}, \alpha_2) = \mathscr{J}(P_\infty, H_{0_\infty}, \alpha_\infty, \hat{\rho}_d, \beta_2), \tag{6.14}$$

$$(\hat{\rho}_1, \hat{p}_1, \delta_1, P_1, H_{0_1}, \alpha_1) = \mathscr{J}(P_\infty, H_{0_\infty}, \alpha_\infty, \hat{\rho}_d, \beta_1), \tag{6.15}$$

$$(\hat{\rho}_3, \hat{p}_3, \delta_3, P_3, H_{0_3}, \alpha_3) = \mathscr{J}(P_1, H_{0_1}, \alpha_1, \hat{\rho}_d/\hat{\rho}_1, \beta_3). \tag{6.16}$$

Note that here we have reverted to the subscripting scheme used for multiple shock wave interactions. Matching the pressure and flow deflection angle across the shear layer that originates at the λ-point we have

$$\hat{p}_2 = \hat{p}_1\hat{p}_3, \tag{6.17}$$

$$\delta_2 = \delta_1 + \delta_3. \tag{6.18}$$

The second inverted λ-point that is observed to appear in the type IV interaction is described by the additional equations

$$\left(\hat{\rho}_4, \hat{p}_4, \delta_4, P_4, H_{0_4}, \alpha_4\right) = \mathscr{J}\left(P_1, H_{0_1}, \alpha_1, \hat{\rho}_d/\hat{\rho}_1, \beta_4\right), \tag{6.19}$$

$$\left(\hat{\rho}_5, \hat{p}_5, \delta_5, P_5, H_{0_5}, \alpha_5\right) = \mathscr{J}\left(P_3, H_{0_3}, \alpha_3, \hat{\rho}_d/(\hat{\rho}_1\hat{\rho}_3), \beta_5\right), \tag{6.20}$$

$$\hat{p}_4 = \hat{p}_3\hat{p}_5, \tag{6.21}$$

$$\delta_4 = \delta_3 + \delta_5. \tag{6.22}$$

Collectively, equations (6.14)–(6.18) and (6.19)–(6.22) represent 34 equations in the 34 variables $\hat{\rho}_{1\text{–}5}$, $\hat{p}_{1\text{–}5}$, $\delta_{1\text{–}5}$, $P_{1\text{–}5}$, $H_{0_{1\text{–}5}}$, $\alpha_{1\text{–}5}$, $\beta_{2\text{–}5}$ and for convenience we choose β_1, P_∞, H_{0_∞}, α_∞ and $\hat{\rho}_d$ as parameters. Solution curves for the density, dissociation levels, shock wave angles, flow deflection angles, and reaction rates are discussed in detail by Sanderson *et al.* (2003). We defer further discussion in the current paper until the heat transfer model has been incorporated.

As was the case for a perfect gas, the important conclusion is that given only the free-stream conditions (P_∞, H_{0_∞}, α_∞, $\hat{\rho}_d$) and the incident shock angle, β_1, all of the wave angles at the two mutually inverted λ-points and hence the flow properties in the supersonic jet are completely determined up to the length scales that remain indeterminate. The solutions that are obtained determine the state of the gas in the jet that impinges on the surface of the body. The undetermined length scales now include the global length scale provided by the interaction of the jet with the body, along with a chemical length scale, $\ell_{d_\infty} = u_\infty/(C\rho_\infty\theta_d^\eta)$.

6.4. *Fay & Riddell stagnation-point heat transfer solution*

Again following the template established in § 1.2, we must consider the problem of modelling the heat fluxes at the jet impingement point. In order to account for the effects of flow thermochemistry we replace the perfect gas stagnation-point boundary layer similarity solution of Cohen & Reshotko (1956) with the non-equilibrium solution of Fay & Riddell (1958):

$$\dot{q} = \zeta_1(\rho_w\mu_w)^{0.1}(\rho_e\mu_e)^{0.4}\sqrt{\left.\frac{\mathrm{d}u_e}{\mathrm{d}x}\right|_0}(h_e - h_w)\left[1 + (Le^{0.52} - 1)\frac{h_d}{h_e}\right]. \tag{6.23}$$

Here $\dot{q}$ is the heat transfer per unit area and time, μ is the viscosity, $\mathrm{d}u_e/\mathrm{d}x|_0$ is the transverse velocity gradient at the outer edge of the boundary layer, Le is the Lewis number, h_d is the chemical enthalpy of the dissociated gas at the edge of the boundary layer and the remaining symbols are defined as before. The subscripts, w and e, denote conditions at the wall and at the outer edge of the boundary layer respectively. The constant of proportionality is $\zeta_1 = 0.94$ for axisymmetric bodies. For planar bodies the value $\zeta_1 = 0.70$ is obtained by extrapolation of results for non-reacting flow (White 1974).

In order to apply this result we must assess the velocity gradient term, $\mathrm{d}u_e/\mathrm{d}x|_0$, at the stagnation point. Conventionally this is done by application of the Newtonian approximation for thin shock layers. Since the density of the outer flow at the stagnation point is constant we have

$$p_e(x) + \tfrac{1}{2}\rho_e u_e(x)^2 = p_e(0).$$

The x-coordinate is measured along the surface of the body with its origin at the stagnation point. Applying L'Hopital's rule in the limit as $x \to 0$ gives the conventional result

$$\left[\left.\frac{\mathrm{d}u_e}{\mathrm{d}x}\right|_0\right]^2 = \frac{-\mathrm{d}^2p/\mathrm{d}x^2|_0}{\rho_e}.$$

The Newtonian approximation gives the pressure distribution as $p_e(x) = \rho_\infty u_\infty^2 \sin^2\beta(x)$. For thin shock layers where the shock inclination, β, is closely approximated by the local surface slope, x/R_c, the stagnation-point velocity gradient becomes

$$\left.\frac{\mathrm{d}u_e}{\mathrm{d}x}\right|_0 = \frac{u_\infty}{R_c}\sqrt{2\rho_\infty/\rho_e} \tag{6.24}$$

where R_c is the radius of *curvature* of the planar or axisymmetric body. Writing the result in this form, the influences of real gas effects are evident in terms of the free-stream velocity and the shock density ratio.

The thin shock layer approximation used to obtain equation (6.24) fails in the limit $R_c \to \infty$. This case is important since it is required for analysis of the blunt-cylinder heat transfer data and also as an approximation for the impingement of the type IV jet where the jet width is much smaller than the body diameter. On dimensional grounds the dependence of the velocity gradient must be

$$\frac{\mathrm{d}u_e/\mathrm{d}x|_0 R_g}{u_\infty} = \mathrm{func}\left(M_\infty, \frac{\rho_e}{\rho_\infty}\right).$$

Note that here R_g is the *geometric* radius of a flat faced body with radius of *curvature* $R_c \to \infty$. In the perfect gas case, that is discussed in some detail by White (1974), the density ratio is determined uniquely by the Mach number and in the hypersonic

limit this asymptotes to $(\gamma+1)/(\gamma-1)$. White (figure 7-7) cites computational and experimental results that give

$$\frac{\mathrm{d}u_e/\mathrm{d}x|_0 R_g}{u_\infty} = 0.15,$$

in the limit $M \to \infty$ for flow of a perfect gas ($\gamma = 1.4$) over a blunt faced body. On the basis of the density dependence exhibited by equation (6.24), and noting that for a cylindrical or spherical body $R_c = R_g$, we extrapolate to the case of a dissociating gas at high Mach numbers:

$$\left.\frac{\mathrm{d}u_e}{\mathrm{d}x}\right|_0 = \zeta_2 \frac{u_\infty}{R_g}\sqrt{2\rho_\infty/\rho_e} \tag{6.25}$$

with,

$$\zeta_2 = \begin{cases} 1, & 1/R_c > 0, \\ 0.15 \times \sqrt{6/2} = 0.26, & 1/R_c = 0. \end{cases} \tag{6.26}$$

The discontinuous limit that is indicated in equation (6.26) is unrealistic and the question of appropriate scalings for the velocity gradient in this regime remains open. This level of approximation is considered adequate for the current conceptual model. Only ratios of the parameters ζ_1 and ζ_2 are contained in the final result and they arise in a form that is not critical to the conclusions of the model.

Following Fay & Riddell (1958), the departure of the stagnation-point boundary layer from equilibrium may be assessed by comparing the lifetime of an atom at the outer edge of the boundary layer with the diffusion time scale across the boundary layer. For the ideal dissociating gas model that we use here the time rate of change of the mass of atoms per unit mixture mass due to recombination is given by the second term of the rate equation (6.11),

$$\left.\frac{\mathrm{d}\alpha}{\mathrm{d}t}\right|_{\mathrm{recomb}} = -C\rho^2 T^\eta \frac{\alpha^2}{\rho_d} = -\ell_d^{-1}\hat{\rho}^2\left(\frac{\hat{T}}{\Theta}\right)^\eta \frac{\alpha^2}{\hat{\rho}_d} u_\infty. \tag{6.27}$$

The dimensionless notation and parameters that are used here are developed in § 6.2. The lifetime of an atom in the boundary layer scales with $\mathrm{d}\alpha/\mathrm{d}t|^{-1}_{\mathrm{recomb}}$. If this is evaluated at the outer edge of the boundary layer and normalized by the velocity gradient (equation (6.25)) at the stagnation point we define a recombination rate parameter, Σ,

$$\Sigma = \frac{\mathrm{d}\alpha/\mathrm{d}t_{\mathrm{recomb}_e}}{\alpha_e^2}\left[\frac{\mathrm{d}u_e}{\mathrm{d}x}\right]_0^{-1} = \frac{D}{\ell_d}\frac{\hat{\rho}_e^{5/2}(\hat{T}_e/\Theta)^\eta}{2\sqrt{2}\zeta_2\hat{\rho}_d}. \tag{6.28}$$

The boundary layer tends to equilibrium for $\Sigma \gg 1$ and is frozen for $\Sigma \ll 1$. The numerical non-equilibrium similarity solutions of Fay & Riddell (1958) indicate that non-equilibrium effects become significant only for values of $\Sigma < 0.1$ when the wall is non-catalytic to the recombination reaction. Table 5 indicates the values of the recombination rate parameter for the current experiments and in all cases the boundary layer is justifiably treated as equilibrium since $\Sigma \gg 0.1$. In this regime recombination occurs at the wall irrespective of the degree of catalysis provided by the model surface (see also § 6.11).

Test condition	A	B	C
$\Sigma\zeta_2\ell_d/D$	0.080	0.018	0.025
ζ_2	1	1	1
ℓ_d	0.19 mm	0.46 mm	0.54 mm
D	40.6 mm	40.6 mm	40.6 mm
Σ	17	1.6	1.9

TABLE 5. Predicted recombination rate parameters for test conditions A, B and C.

6.5. *Normalization of the stagnation-point heat flux*

The stagnation point heat transfer rate given by equation (6.23) may be expressed as a Stanton number,

$$St_{body} = \frac{\dot{q}}{\rho_\infty u_\infty h_{0_\infty}} = \zeta_1 \frac{(\rho_w\mu_w)^{0.1}(\rho_e\mu_e)^{0.4}}{\rho_\infty u_\infty}\left[1+0.2\frac{\alpha_e}{H_{0_\infty}}\right]\sqrt{\left.\frac{\mathrm{d}u_e}{\mathrm{d}x}\right|_0}.$$

The Lewis number has been taken as $Le = 1.4$ and the enthalpy of dissociation is given by

$$\frac{h_d}{h_e} = \frac{\alpha_e(2m/k\theta_d)^{-1}}{h_e} = \frac{\alpha_e}{H_{0_\infty}}.$$

If the velocity gradient is introduced from equation (6.25) this becomes

$$St_{body} = 2^{3/4}\sqrt{\frac{\zeta_1^2\zeta_2}{Re_\infty}}(\hat{\rho}_w\hat{\mu}_w)^{0.1}\hat{\mu}_e^{0.4}\hat{\rho}_e^{0.15}\left[1+0.2\frac{\alpha_e}{H_{0_\infty}}\right]. \tag{6.29}$$

The Reynolds number is defined with respect to the body diameter and the free-stream conditions, $Re_\infty = \rho_\infty u_\infty D/\mu_\infty$. The Sutherland viscosity formula is used to evaluate μ_∞. In order to simplify treatment of the type IV jet model a power law model is used for the viscosity across the boundary layer (White 1974):

$$\hat{\mu}_w = \hat{T}_w^{0.7}, \qquad \hat{\mu}_e = \hat{T}_e^{0.7}.$$

Since the pressure at the edge of the boundary layer is given by the Newtonian approximation we obtain $\hat{p}_e = \rho_\infty u_\infty^2/p_\infty = 1/P_\infty$ and using the IDG thermal equation of state (Sanderson, *et al.* 2003),

$$\hat{T}_e = \frac{1+\alpha_\infty}{P_\infty\hat{\rho}_e(1+\alpha_e)}.$$

Further, the pressure across the boundary layer is constant, $\hat{p}_w = \hat{p}_e = 1/P_\infty$, and the thermal equation of state gives the wall density ratio,

$$\hat{\rho}_w = \frac{1+\alpha_\infty}{P_\infty\hat{T}_w}.$$

Since the wall temperature is low and the boundary layer is in equilibrium we have taken $\alpha_w = 0$. Substituting these dependences into equation (6.29) we obtain the Stanton number as a function of the relevant dimensionless parameters,

$$St_{body} = 2^{3/4}\sqrt{\frac{\zeta_1^2\zeta_2}{Re_\infty}}\left(\frac{1+\alpha_\infty}{P_\infty}\right)^{0.38}(1+\alpha_e)^{-0.28}\hat{T}_w^{-0.03}\hat{\rho}_e^{-0.13}\left[1+0.2\frac{\alpha_e}{H_{0_\infty}}\right]. \tag{6.30}$$

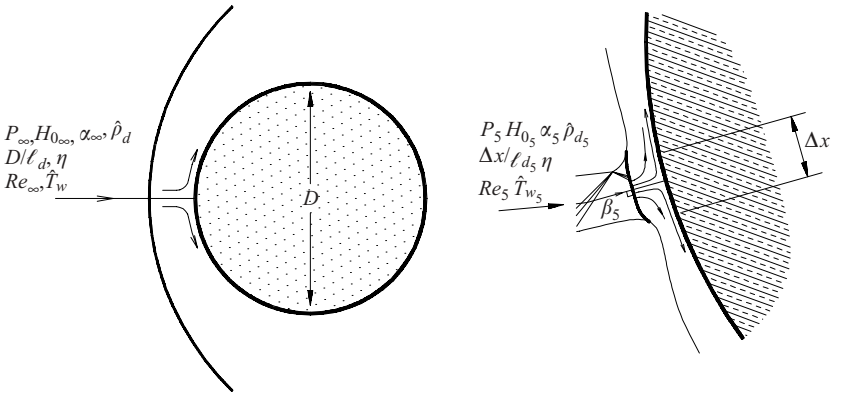

FIGURE 13. Adaption of the Fay & Riddell stagnation-point solution to the jet impingement problem.

The complete dimensionless dependence of the stagnation-point heating problem as it is modelled here becomes $St_{body}(P_\infty, H_{0_\infty}, \alpha_\infty, \hat{\rho}_d, D/\ell_d, \eta, Re_\infty, \hat{T}_w)$. The remaining variables, α_e and $\hat{\rho}_e$, are determined from the equilibrium normal shock solution (outlined in § 6.2) in terms of the same set of parameters. Variation of the flow variables as the subsonic flow decelerates to the stagnation point is neglected since the Mach number is low.

6.6. *Type IV jet heat transfer solution*

Following the pattern of Edney (1968*a*) we adapt the expression (6.30) to study the influence of real gas effects on the shock impingement problem (see figure 13). The parameters describing the free-stream conditions are given by the inviscid shock interaction solution (see § 6.3). The conditions upstream of the normal shock at the base of the jet are taken to be those existing at state 5, behind the third wave produced at the inverted λ-point. Subsequent expansion waves are neglected based on the experimentally observed peak heating configuration. This configuration minimizes the strength of the terminating jet shock, thereby minimizing further entropy rise along the stagnation streamline and ensuring the maximum heating condition. We then have

$$St_{jet} = 2^{3/4}\sqrt{\frac{\zeta_{1_{jet}}^2\,\zeta_{2_{jet}}}{Re_5}}\left(\frac{1+\alpha_5}{P_5}\right)^{0.38}(1+\alpha_6)^{-0.28}\hat{T}_{w_5}^{-0.03}\hat{\rho}_6^{-0.13}\left[1+0.2\frac{\alpha_6}{H_0}\right]. \tag{6.31}$$

As before, subsonic variations of the equilibrium state, 6, behind the terminating jet shock are neglected as the flow decelerates to the stagnation-point. The intensification of the heat transfer as a result of jet impingement is

$$\frac{\dot{q}_{jet}}{\dot{q}_{body}} = \frac{St_{jet}\rho_5 u_5 h_{0_5}}{St_{body}\rho_\infty u_\infty h_{0_\infty}} = \frac{St_{jet}}{St_{body}}\hat{\rho}_5\hat{\rho}_3\hat{\rho}_1\sqrt{\frac{K_5}{K_\infty}}. \tag{6.32}$$

All of the terms in equations (6.30) and (6.31) that are necessary to evaluate this expression are available from the inviscid jet solution with the exception of Re_5. The ratio, $\hat{T}_{w_5}/\hat{T}_{w_\infty}$, arises and this is determined by the thermal equation of state to be

$$\frac{\hat{T}_{w_5}}{\hat{T}_{w_\infty}} = \frac{T_\infty}{T_1}\frac{T_1}{T_3}\frac{T_3}{T_5} = \frac{\hat{\rho}_5\hat{\rho}_3\hat{\rho}_1}{\hat{\rho}_5\hat{\rho}_3\hat{\rho}_1}\left(\frac{1+\alpha_5}{1+\alpha_\infty}\right). \tag{6.33}$$

The ratio of the Reynolds numbers is similarly determined since we have assumed a power law dependence for the viscosity:

$$\frac{Re_5}{Re_\infty} = \frac{\rho_5 u_5 \mu_\infty \Delta x}{\rho_\infty u_\infty \mu_5 D} = \hat{\rho}_5 \hat{\rho}_3 \hat{\rho}_1 \sqrt{\frac{K_5}{K_\infty}} \frac{\Delta x}{D} \left(\frac{\hat{T}_{w_5}}{\hat{T}_{w_\infty}} \right)^{0.7}. \tag{6.34}$$

Substituting equations (6.31), (6.30), (6.33) and (6.34) into equation (6.32) we obtain the following expression for the increase in heat transfer produced by the type IV interaction for an ideal dissociating gas:

$$\frac{\dot{q}_{jet}}{\dot{q}_{body}} = \sqrt{\frac{\zeta_{1_{jet}}^2 \zeta_{2_{jet}}}{\zeta_{1_{body}}^2 \zeta_{2_{body}}} \frac{D}{\Delta x}} \left(\frac{K_5}{K_\infty} \right)^{0.25} (\hat{\rho}_5 \hat{\rho}_3 \hat{\rho}_1)^{0.12} (\hat{p}_5 \hat{p}_3 \hat{p}_1)^{0.38}$$
$$\times \left(\frac{P_\infty}{P_5} \right)^{0.38} \left(\frac{1+\alpha_6}{1+\alpha_e} \right)^{-0.28} \left(\frac{\hat{\rho}_6}{\hat{\rho}_e} \right)^{-0.13} \left[\frac{H_0 + 0.2\alpha_6}{H_0 + 0.2\alpha_e} \right]. \tag{6.35}$$

6.7. *Discussion*

Observe that although the heat transfer rates vary inversely with the square root of the Reynolds number in equations (6.30) and (6.31), the intensification of the heat transfer due to jet impingement in equation (6.35) is independent of the Reynolds number. This is consistent with the experimental observations of Wieting & Holden (1989) at low enthalpies. Limited variation in the heat transfer intensification was observed as the Reynolds number was changed with the remaining parameters held nearly constant.

The last three factors of equation (6.35) are close to unity. This is a consequence of the conservation of stagnation-enthalpy at all points in the flow and the weak additional dependence of the stagnation-point dissociation level on density. To a very good approximation $\alpha_6 \approx \alpha_e$. The ratio of the normal shock density ratios, $\hat{\rho}_6/\hat{\rho}_e$, is only slightly less than unity provided both shock waves remain strong and the small exponent, -0.13, reduces its influence. The square root dependence on the geometrical factors, $D/\Delta x$ and $\zeta_{1_{jet}}^2 \zeta_{2_{jet}}/(\zeta_{1_{body}}^2 \zeta_{2_{body}})$, is explicit. The remaining four factors demonstrate intensification caused by increases in the jet specific kinetic energy, density, pressure and Mach number respectively.

6.8. *Numerical solutions*

The four factors that are discussed above control most of the interesting effects. Their behaviour is determined by the two λ-point solutions of § 6.3. Equations (6.14)–(6.18), (6.19)–(6.22) and (6.35) determine the solution, which has the form

$$\frac{\dot{q}_{jet}}{\dot{q}_{body}} \sqrt{\frac{\Delta x}{D} \frac{\zeta_{1_{body}}^2 \zeta_{2_{body}}}{\zeta_{1_{jet}}^2 \zeta_{2_{jet}}}} = fnc(P_\infty, H_{0_\infty}, \hat{\rho}_d, \alpha_\infty, \beta_1). \tag{6.36}$$

The equations are solved using Newton's method and the solution is continued in H_{0_∞} for typical values of the remaining parameters. The term under the square root in (6.36) specializes the result for a particular geometry and remains indeterminate. The influence of dissociation chemistry appears principally through the parameter H_{0_∞}. Finite rate effects are evaluated by considering three different thermodynamic models to close the system of equations:

(*a*) a chemically frozen solution with all shock waves determined by function (6.13) and equation (6.8),

(*b*) a full equilibrium solution with all shock waves determined by function (6.13) in combination with equations (6.7) and (6.9);

(*c*) an approximate non-equilibrium solution under the assumption

$$\frac{\mathrm{d}\alpha_1}{\mathrm{d}\hat{x}_\infty}, \frac{\mathrm{d}\alpha_3}{\mathrm{d}\hat{x}_\infty}, \frac{\mathrm{d}\alpha_5}{\mathrm{d}\hat{x}_\infty} \ll \frac{\mathrm{d}\alpha_2}{\mathrm{d}\hat{x}_\infty}, \frac{\mathrm{d}\alpha_4}{\mathrm{d}\hat{x}_\infty}, \frac{\mathrm{d}\alpha_6}{\mathrm{d}\hat{x}_\infty}, \tag{6.37}$$

where only shocks 2, 4 and 6 are allowed to come to equilibrium and shocks 1, 3 and 5 remain chemically frozen.

The non-equilibrium approximation is motivated by the observation of widely differing shock strengths in Mach reflection by Hornung, Oertel & Sandeman (1979) and the computations of Carlson & Wilmoth (1994) and Brück (1995) that indicate suppressed chemical reaction rates in the supersonic jet. The validity of the non-equilibrium approximation may be assessed from the requirement that the reaction rate downstream of the jet shocks (1, 3 and 5) be small relative to that behind the undisturbed bow shock (i.e. $(\mathrm{d}\alpha_5/\mathrm{d}\hat{x}_\infty)/(\mathrm{d}\alpha_e/\mathrm{d}\hat{x}_\infty) \ll 1$) according to the rate expression (6.11). The influences of α_∞ and $\hat{\rho}_d$ are numerically significant but secondary in terms of demonstrating the essential behaviour. The claim therefore is that the solution curves plotted using the universal form, (6.36), in figures 14 and 15 below, illustrate the main mechanisms involved.

6.9. *Features of the solutions*

The influence of real gas effects on the shock impingement heating problem may be observed in figure 14. The difference between the frozen and equilibrium solutions increases with dimensionless stagnation enthalpy as a consequence of the increasing density ratio across the jet shocks, 3 and 5, caused by dissociation. This effect is absent in the non-equilibrium solution that in fact decreases slightly with respect to the frozen solution. Since $\alpha_6 \approx \alpha_e$ and $\alpha_5 = 0$, the effects of dissociation on the normal wave, 6, and the undisturbed bow shock are similar. This limits the deviation of the frozen and non-equilibrium heat transfer ratios. The significance of real gas effects is seen to increase with decreasing Mach number (or increasing P_∞). Figure 14(*c*) demonstrates that the validity of the non-equilibrium approximation improves with increasing Mach number and decreasing stagnation enthalpy.

Existing models predict that the heat transfer intensification increases with impinging shock strength and eventually reaches a local maximum before decreasing for still stronger impinging waves. This trend is reproduced by the behaviour of the solutions obtained at moderate Mach number ($M_\infty = 8.7$ assuming $\gamma = 4/3$) in figure 15. Note that as β_1 approaches the local maxima of the different solution curves, the relative influence of real gas effects declines whereas the relative influence of real gas effects is quite large for shock angles either side of the maxima. The reaction rate curve shown in figure 15 indicates that non-equilibrium effects are most significant for weak (but finite) strength waves. For vanishingly weak waves the jet reaction rate increases and this effect becomes more abrupt as the Mach number increases. At higher Mach numbers the reaction rate in the jet is depressed over a wider range of shock angles. End points of the various solution curves correspond to conditions at which the flow downstream of shock 5 becomes subsonic with respect to the frozen speed of sound.

6.10. *Interpretation of the mechanisms*

The thermochemical influences that are discussed above may be understood from the variations of the jet shock strengths that are demonstrated in figure 16 for frozen

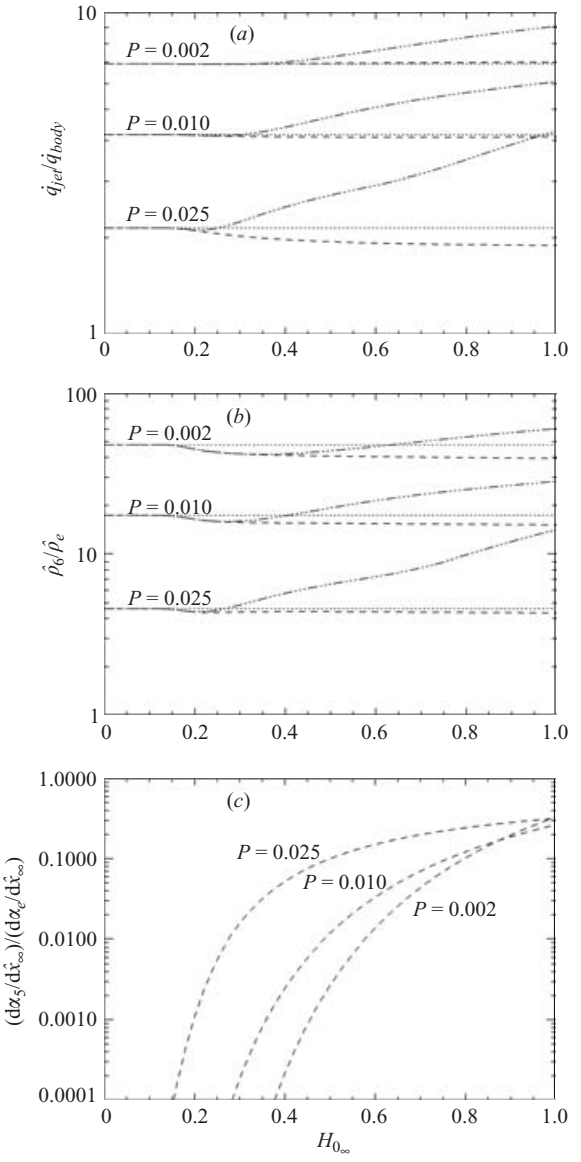

FIGURE 14. Influence of dimensionless stagnation enthalpy, H_{0_∞}, Mach number, $\sim 1/\sqrt{P_\infty}$ and reaction rate on type IV heat transfer intensification. (*a*) Heat transfer intensification, $(\dot{q}_{jet}/\dot{q}_{body})\sqrt{(\Delta x/D)(\zeta^2_{1_{body}}\zeta_{2_{body}}/\zeta^2_{1_{jet}}\zeta_{2_{jet}})}$; (*b*) stagnation density intensification, $\hat{\rho}_6/\hat{\rho}_e$ and (*c*) jet reaction rate ratio, $(d\alpha_5/d\hat{x}_\infty)/(d\alpha_e/d\hat{x}_\infty)$. ·····, The frozen solutions; — ··· —, the equilibrium solutions; – – –, the nonequilibrium solutions in the limit $d\alpha_1/d\hat{x}_\infty, d\alpha_3/d\hat{x}_\infty, d\alpha_5/d\hat{x}_\infty \ll d\alpha_2/d\hat{x}_\infty, d\alpha_4/d\hat{x}_\infty, d\alpha_6/d\hat{x}_\infty$. The parameters are $P_\infty = 0.002, 0.010, 0.025$, $\hat{\rho}_d = 1 \times 10^7$, $\alpha_\infty = 0$ and $\beta_1 = 16°$.

chemistry and conditions that match figure 15. At the intermediate shock angles where peak heating occurs, $\beta_1 = 15°$ and $\beta_1 = 20°$, the strengths of the jet shocks (1,3 and 5) are balanced to produce the maximum compression and heat transfer intensification. For very weak impinging waves, $\beta_1 = 8°$, we see that the shock connecting the two λ-points becomes disproportionately strong. In the case of a strong impinging wave,

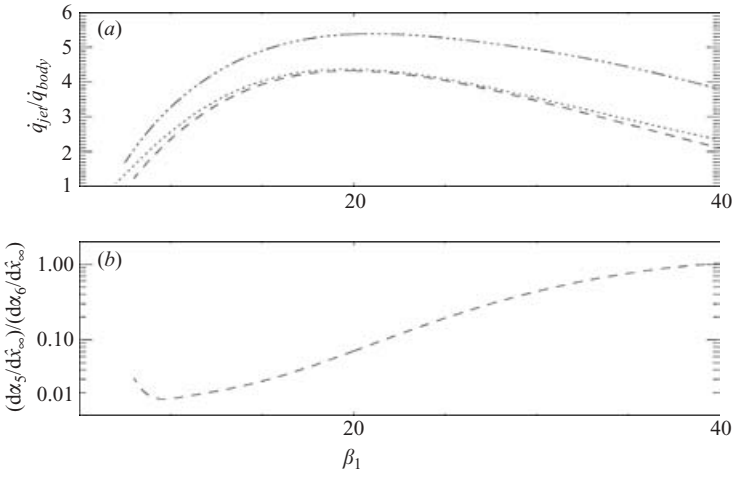

FIGURE 15. Influence of impinging shock wave angle, β_1, and reaction rate on type IV heat transfer intensification at moderate Mach number; $P_\infty = 0.010$. (*a*) Heat transfer intensification, $(\dot{q}_{jet}/\dot{q}_{body})\sqrt{(\Delta x/D)(\zeta_{1_{body}}^2 \zeta_{2_{body}}/\zeta_{1_{jet}}^2 \zeta_{2_{jet}})}$ and (*b*) jet reaction rate ratio, $d\alpha_5/d\hat{x}_\infty/d\alpha_e/d\hat{x}_\infty$. · · · · ·, The frozen solution; — · · · —, the equilibrium solution; – – –, the non-equilibrium solution in the limit $d\alpha_1/d\hat{x}_\infty, d\alpha_3/d\hat{x}_\infty, d\alpha_5/d\hat{x}_\infty \ll d\alpha_2/d\hat{x}_\infty, d\alpha_4/d\hat{x}_\infty, d\alpha_6/d\hat{x}_\infty$. The parameters are $H_{0_\infty} = 0.6$, $\hat{\rho}_d = 1 \times 10^7$ and $\alpha_\infty = 0$.

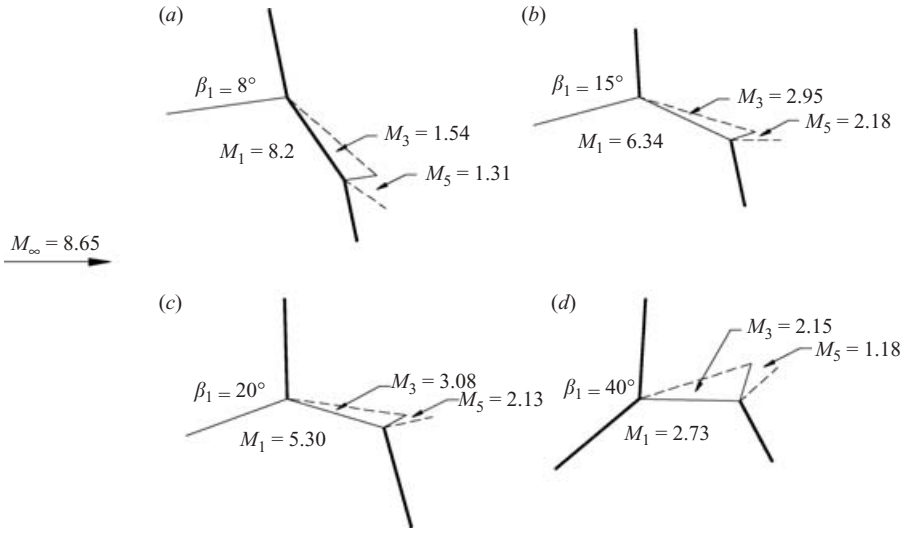

FIGURE 16. Variation of type IV jet shock strengths with impinging shock angle, β_1. Free-stream conditions for the frozen solutions are $P_\infty = 0.010$, $\alpha_\infty = 0$; and (*a*) $\beta_1 = 8°$, (*b*) 15°, (*c*) 20°, (*d*) 40°. The shock angles and flow deflection angles shown are to scale.

$\beta_1 = 40°$, the compression across the incident wave dominates. Maximum heating results therefore from a balancing of the jet shock strengths. The key conclusion is that this balance simultaneously reduces the relative influence of equilibrium real gas effects and depresses the jet reaction rate. This follows from the results discussed by Sanderson *et al.* (2003) who demonstrated the limited extent and rate of the

dissociation reaction downstream of even moderate strength oblique shock waves. Real gas effects become significant at lower Mach numbers and away from the peak heating shock angle when at least one of the jet shocks causes significant dissociation.

6.11. *Dissociation and recombination rate parameters for the type IV jet*

As a final check on the validity of the assumptions of the model we consider the dissociation and recombination rate parameters for the type IV jet. The definitions of these parameters follow from the approximate form of Δ_D given by Sanderson *et al.* (2003) and equation (6.28) where the free-stream conditions are now taken to be those downstream of the jet shock system (figure 13). It is convenient to represent these parameters as ratios of the form

$$\frac{\Delta_5}{\Delta_\infty}\frac{D}{\Delta x} = \frac{\mathrm{d}\alpha_6/\mathrm{d}\hat{x}_5}{\mathrm{d}\alpha_e/\mathrm{d}\hat{x}_\infty}\sqrt{\frac{K_\infty}{K_5}}\hat{\rho}_5\hat{\rho}_3\hat{\rho}_1\left(\frac{\hat{\rho}_{f_e}}{\hat{\rho}_{f_6}}\right), \tag{6.38}$$

where the characteristic reaction lengths have been renormalized according to methodology of Sanderson *et al.* (2003). The reaction rates, $\mathrm{d}\alpha_6/\mathrm{d}\hat{x}_5$ and $\mathrm{d}\alpha_e/\mathrm{d}\hat{x}_\infty$, along with the frozen shock density ratios, $\hat{\rho}_{f_e}$ and $\hat{\rho}_{f_6}$, are obtained from the type IV jet solution given in § 6.3. The ratio of the recombination rate parameters follows from equation (6.28):

$$\frac{\Sigma_5}{\Sigma_\infty}\frac{D\zeta_{2_{jet}}}{\Delta x\zeta_{2_{body}}} = \frac{\sigma_5}{\sigma_\infty}\sqrt{\frac{K_\infty}{K_5}}\hat{\rho}_5\hat{\rho}_3\hat{\rho}_1, \tag{6.39}$$

where $\sigma_5 = \hat{\rho}_6^{5/2}(\hat{T}_6/\Theta_5)^\eta/\hat{\rho}_{d_5}$ and $\sigma_\infty = \hat{\rho}_e^{5/2}(\hat{T}_e/\Theta_\infty)^\eta/\hat{\rho}_{d_\infty}$ are determined from the type IV jet solution (see § 6.3). The temperature ratios in these expressions are given by equation (6.12).

Figure 17 shows the jet dissociation rate parameter for the free-stream conditions that correspond to figure 15. Increases in the dissociation rate due to the higher density at the jet impingement point are offset by the ratio $\Delta x/D$. The net effect is that the jet shock dissociation rate parameter is similar to the undisturbed bow shock rate parameter. Due to relaxation that occurs in the jet, the equilibrium curve lies below the non-equilibrium curve. This also explains the strong dip in the equilibrium solution for weak impinging waves where the unbalanced oblique jet shock system causes significant dissociation.

The recombination rate parameter ratios are observed to vary with the square of the dissociation rate parameter ratios. This is consistent with the scaling of the recombination rate with the square of the density. We conclude that the jet boundary layer lies significantly closer to equilibrium than that on the undisturbed blunt body. For conditions where $\Sigma_\infty \ll 1$ but $\Sigma_5 \approx 1$, this may produce an additional increase in the heat transfer rate, beyond that produced by the type IV interaction alone, if the body surface is non-catalytic to the recombination reaction. This scenario would arise in experiments conducted at high enthalpy but at low pressure (see also Carlson & Wilmoth 1994).

For low values of the recombination rate parameters, or where surface catalysis gives rise to non-equilibrium recombination in the stagnation-point boundary layer, equation (6.23) and the results that follow from it are not applicable. Here the jet shock solution must be coupled with explicit numerical solutions for the non-equilibrium recombination (see Fay & Riddell 1958).

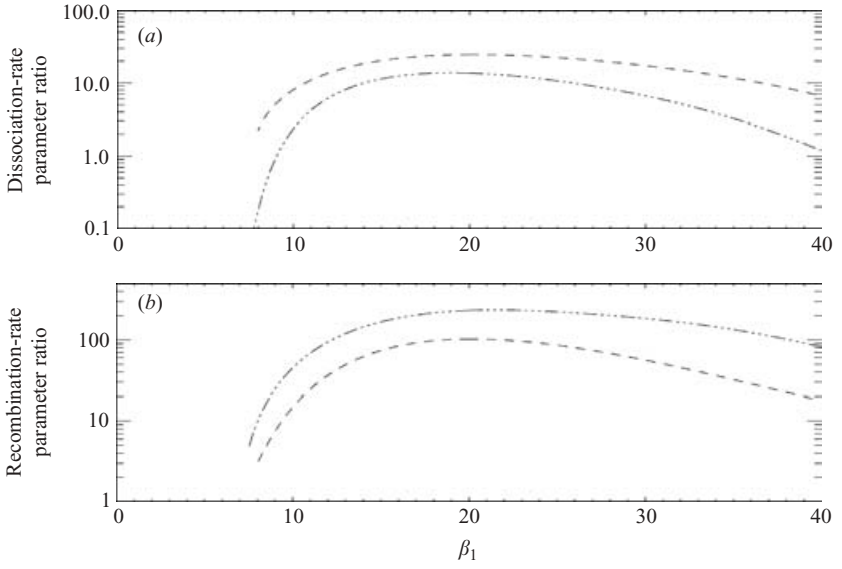

FIGURE 17. Reaction rate parameters for the type IV jet stagnation point. (*a*) The ratio of the dissociation rate parameters in the form, $(\Delta_5/\Delta_\infty)(D/\Delta x)$, (*b*) the ratio of the recombination rate parameters, $(\Sigma_5/\Sigma_\infty)(D\zeta_{2_{jet}}/\Delta x\zeta_{2_{body}})$. ——···——, The equilibrium solutions; ————, the non-equilibrium solutions. The free-stream conditions are $P_\infty = 0.010$, $H_{0_\infty} = 0.6$, $\hat{\rho}_{d\infty} = 1 \times 10^7$, $\alpha_\infty = 0$.

6.12. *Comparison with existing models*

Edney (1968*a*) discussed the type IV model data in terms of the jet pressure ratio. For the current model density and heat transfer ratios were better indicators of the influence of real gas effects, since it is known that pressure ratio is only weakly sensitive to non-equilibrium dissociation effects. Provided that the jet Mach number remains high we can approximate the intensification of the stagnation pressure by

$$\frac{p_{6_0}}{p_e} = \frac{\rho_5 u_5^2}{\rho_\infty u_\infty^2} = \hat{\rho}_5 \hat{\rho}_3 \hat{\rho}_1 \frac{K_5}{K_\infty}.$$

Using this form, figure 3 compares the current frozen solution with the results of Edney (1968*a*). The real gas shock solution (equations (6.7)–(6.13)) has been verified against independent calculations for a single wave. The curve for $\gamma = 1.2$ in figure 3 demonstrates Edney's prediction of greatly increased heat transfer at high enthalpies. This value is typical for stagnation temperatures in the range 8000–12000 K that are studied here. Comparing figure 3 with figure 15 we see that the constant-γ model considerably over-estimates the influence of real gas effects. This occurs because the density ratio across all shock waves is increased uniformly as γ is reduced. This includes the jet shock waves that determine the heat transfer intensification and across these waves the influence of real gas effects is limited.

7. Comparison of model with experimental data

Table 6 contains the detailed predictions of the model for the free-stream conditions that were used in the experimental portion of this work. The parameters for the computation, P_∞, H_{0_∞}, $\hat{\rho}_d$, α_∞ and β_1, are given in table 1. No other adjustable parameters appear in the model, other than the indeterminate geometrical terms that

	A			B			C		
	Frzn	Non-eq.	Equil.	Frzn	Non-eq.	Equil.	Frzn	Non-eq.	Equil.
β_1 (deg.)	14.25	14.25	14.25	15	15	15	16	16	16
β_2 (deg.)	−87.1	−87.1	−87.1	−84.7	−86.3	−86.2	−83.1	−86.1	−85.7
β_3 (deg.)	−33.1	−33.1	−33.1	−43.5	−45.1	−44.9	−48.4	−51.6	−49.3
δ_1 (deg.)	10.2	10.2	10.2	8.12	8.12	8.12	7.31	7.31	7.31
δ_2 (deg.)	−15.5	−15.5	−15.5	−24.3	−25.5	−25.7	−27.2	−29.2	−31.5
$\frac{\hat{\rho}_6}{\hat{\rho}_e}$	21.5	21.5	21.5	7.05	6.53	7.13	4.12	3.59	5.61
$\frac{d\alpha_5}{d\hat{x}_\infty} \Big/ \frac{d\alpha_e}{d\hat{x}_\infty}$	—	—	—	.0045	.0089	.0023	.059	.119	.00065
$\frac{\dot{q}_{jet}}{\dot{q}_{body}} \times \left(\frac{\Delta x}{D} \frac{\zeta_{1_{body}}^2 \zeta_{2_{body}}}{\zeta_{1_{jet}}^2 \zeta_{2_{jet}}} \right)^{1/2}$	4.63	4.63	4.63	2.66	2.54	2.75	2.03	1.82	2.52
χ/D	0.218	0.218	0.218	0.186	0.186	0.186	0.173	0.173	0.173
$\lvert\beta_3 + \delta_1 - \delta_2\rvert$ (deg.)	7.4	7.4	7.4	11.1	11.5	11.1	13.9	15.1	10.5
$\frac{\dot{q}_{jet}}{\dot{q}_{body}}$	14.1	14.1	14.1	7.16	6.73	7.41	5.07	4.37	7.23

TABLE 6. Model predictions for conditions A, B and C respectively, for frozen, non-equilibrium and equilibrium conditions.

are estimated below. The heat transfer rate is predicted by the model in the universal form

$$\frac{\dot{q}_{jet}}{\dot{q}_{body}} \sqrt{\frac{\Delta x}{D} \frac{\zeta_{1_{body}}^2 \zeta_{2_{body}}}{\zeta_{1_{jet}}^2 \zeta_{2_{jet}}}}. \tag{7.1}$$

Both the undisturbed body flow and the impinging jet are planar so that $\zeta_{1_{body}} = \zeta_{1_{jet}} = 1$ (equation (6.23)). Equation (6.26) gives $\zeta_{2_{body}} = 1$ and $\zeta_{2_{jet}} = 0.26$. Since the experimental results indicate that the peak type IV heating occurs when the second λ-point lies close to the body, before the jet narrows at higher impingement locations, we propose the following as an unbiased scaling of the jet width to body diameter ratio:

$$\frac{\Delta x}{D} = \frac{\chi}{D} \sin(|\beta_3 + \delta_1 - \delta_2|). \tag{7.2}$$

This relationship scales the jet width with the undisturbed shock standoff distance, χ, and the divergence angle of the oblique wave and shear layer at the λ-point (see figure 1). All of the quantities appearing in equation (7.2) may be predicted *a priori*. By choosing to scale the interaction in this manner we predict the largest possible value of heat transfer intensification that might arise for a given set of dimensionless parameters. Improved geometrical scalings may be possible based on the work of Frame & Lewis (1997). Examination of the jet divergence angle, $|\beta_3 + \delta_1 - \delta_2|$, in table 6 reveals an additional influence of finite rate effects whereby the decreased density of the jet causes a divergence of the shock and shear layer. This translates into a further reduction in the heat flux that is not encompassed by the universal form, (7.1).

Whilst the calculations were based on the measured incident shock angles, β_1, the flow deflection angles computed from them are somewhat larger than the actual shock

Test condition	A	B	C
Undisturbed fringe shift	13 ± 1	10.5 ± 1	9 ± 1
Type IV fringe shift	55 ± 2	29.5 ± 1	27 ± 1
Ratio	4.2 ± 0.5	2.81 ± 0.4	3.0 ± 0.4
Predicted $\hat{\rho}_6/\hat{\rho}_e$			
Frozen	21.5	7.05	4.12
Non-equilibrium	—	6.53	3.59
Equilibrium	—	7.13	5.61

TABLE 7. Comparison of measured and predicted stagnation density intensification for type IV flows with cylindrical model.

generator angle of 6°. The discrepancy is consistent with nozzle flow non-uniformity and an over-prediction of the Mach number caused by running a constant-area-ratio shock tunnel nozzle at low-enthalpy off-design conditions. Observe the decline of the discrepancy with increasing stagnation enthalpy as the nozzle approaches the high-enthalpy design condition (see Sanderson 1995 for discussion).

7.1. *Heat flux data*

The results contained in table 6 reflect the negligible dissociation levels for condition A. The peak heat transfer rate is consistent with the heat transfer measurements summarized in figure 11. Non-equilibrium effects were most pronounced for condition B where the reaction rate in the supersonic jet was two orders of magnitude less than that behind the undisturbed bow shock. The influence of this on the measurable quantities was only slight since the dissociation levels remain small. Despite the limited number of data points obtained at condition B, the trends predicted by the model are confirmed by the data in figure 11. The effect of dissociation chemistry is most obvious at condition C (see table 6). Significant dissociation occurs and this is reflected in the peak density and heat transfer ratios. Chemical non-equilibrium produces a decrease in these quantities; however the depression of the jet reaction rate is only moderate. Since the reaction rate parameter was large for the undisturbed flow ($\Delta = 21$), the jet should remain close to equilibrium. Figure 11 indicates heat transfer rates that are consistent with this interpretation. Although the model appears to predict the heating rates for the current conditions quite reliably, further experiments spanning a range of reaction rate parameters would be required to discern the non-equilibrium behaviour.

7.2. *Density data*

The peak interferometric fringe shift for the type IV flow was measured from the holograms shown in figure 8. Table 7 lists the ratios of the peak fringe shifts relative to the stagnation-point values without shock impingement. Estimates of the error include only the precision of the measurement. Additional systematic error was introduced through line-of-sight integration of spanwise variations of the jet structure. The peak fringe shifts are therefore smaller than the density ratios predicted by the model.

8. Conclusions

A series of experiments was conducted in the T5 free-piston driver shock tunnel to determine the quantitative effects of high-enthalpy thermochemistry on the shock impingement heating problem. By studying the nominally two-dimensional mean flow about a cylinder with a coplanar impinging shock wave the topology of the problem

was simplified so that it could be observed directly by holographic interferometry. Interferograms obtained for three different test conditions indicated that existing predictions of greatly increased stagnation density at high enthalpy were not realized. Time-resolved heat transfer measurements confirmed this observation and were correlated, along with data from previous studies, with the independent dimensionless variables. It was demonstrated that 85% of the variability in the heat transfer data was correlated by variations in free-stream Mach number and impinging shock wave angle. No statistically significant trends with Reynolds number or stagnation enthalpy were resolvable. A simple correlation of the heat transfer data was determined for practical design purposes in the weak impinging shock regime.

Temporal fluctuations of the impinging jet were observed at all test conditions and a Strouhal number was estimated at the low-enthalpy test condition. Variations of the tunnel test conditions during the test time limited the quality of the spectra at high enthalpies. Whilst it was not possible to conclusively discount the effect of free-stream perturbations, the data exhibited features that have been observed in numerical studies. The observed Strouhal number was consistent with the limited existing data.

The current experiments exposed deficiencies in previous variable-γ models of the shock impingement phenomenon that over-predict the experimentally observed heat transfer rates and densities at high enthalpy. In order to reconcile the experimental observations with prior analyses, the jet shock system was modelled using the ideal dissociating gas approximation and a non-equilibrium stagnation-point similarity solution was applied to describe the impingement of the jet on the body. Careful non-dimensionalization of the problem led to a tractable formulation and identification of the important parameters. The results were used to demonstrate generic influences of real gas effects on the shock impingement problem. Widely differing shock strengths produced at the λ-points result in rapid dissociation downstream of the strong bow shock wave whereas the extents and rates of dissociation for the weak jet shocks are depressed.

The improved model led to the conclusion that peak heating occurs when the strengths of the oblique shock waves in the supersonic jet are balanced to minimize the entropy rise along the stagnation streamline. This minimum entropy condition concomitantly reduces the influence of equilibrium real gas effects and depresses the jet reaction rate at the peak heating condition. Real gas effects were shown to be important when the balance of the oblique shock waves is disturbed and this occurs at lower Mach numbers and for impinging shock angles away from that which produces peak heating.

The model accurately reproduced the experimentally observed heat transfer rates using *a priori* estimated parameters. Accurate predictions of the heat transfer rates should be possible for conditions where turbulent diffusion of the supersonic jet is unimportant. Relative trends of the interferometric data at the different conditions were consistent with the model predictions; however quantitative comparisons were hindered by variations in the jet impingement location across the span of the model.

A non-equilibrium approximation was introduced that applies under conditions where the jet shocks remain weak with respect to the undisturbed bow shock. Within the scope of the approximation non-monotonic behaviour was predicted with the reaction rate parameter. Although the model predicts the independent effects of finite rate kinetics and total enthalpy, experimental discrimination of these independent influences would require additional experiments conducted over a broader range of shock tunnel test conditions.

Regrettably, Professor Brad Sturtevant passed away on 20 October 2000 during the preparation of this archival publication. It is clear that this work has benefited immeasurably from our co-author's insight, guidance and characteristic thoroughness.

The first author is grateful for assistance received from the Darryl G. Greenamyer Fellowship and C. L. Powell Fellowship funds. This work was supported by AFOSR Grant Nos. F49620-92-J-0110 and F49620-93-1-0338.

REFERENCES

Borovoy, V. Ya., Chinilov, A. Yu., Gusev, V. N., Strminskaya, I. V., Delery, J. & Chanetz, B. 1997 Interference between a cylindrical bow shock and a plane oblique shock. *AIAA J.* **35**, 1721–1728.

Brück, S. 1995 Investigation of shock-shock interactions in hypersonic reentry flows. *Proc. 20th Intl Symp. on Shock Waves, Pasadena*, Vol. I (ed. B. Sturtevant, J. Shepherd & H. G. Hornung), pp. 215–220. World Scientific.

Carlson, A. B. & Wilmoth, R. G. 1994 Monte Carlo simulation of a near continuum shock-shock interaction problem. *J. Spacecraft Rockets* **31**, 25–30.

Cohen, C. B. & Reshotko, E. 1956 Similar solutions for the compressible laminar boundary layer with heat transfer and pressure gradient. *NACA Rep.* 1293.

Collins, J. A. 1981 *Failure of Materials in Mechanical Design.* John Wiley & Sons.

Courant, R. & Friedrichs, K. O. 1948 *Supersonic Flow and Shock Waves.* Interscience.

Davies, L. & Wilson, J. L. 1969 Influence of reflected shock and boundary-layer Interaction on shock tube flows. *Phys. Fluids*, Supplement I, I-37–43.

Edney, B. E. 1968*a* Anomalous heat transfer and pressure distributions on blunt bodies at hypersonic speeds in the presence of an impinging shock. *FFA Rep.* 115.

Edney, B. E. 1968*b* Effects of shock impingement on the heat transfer around blunt bodies. *AIAA J* **6**, 15–21.

Fay, J. A. & Riddell, F. R. 1958 Theory of stagnation point heat transfer in dissociated air. *J. Aeronaut. Sci.* **25**, 73–85.

Frame, M. J. & Lewis, M. J. 1997 Analytical solution of the Type IV shock interaction. *J. Prop. Power* **13**, 601–609.

Freeman, N. C. 1958 Non-equilibrium flow of an ideal dissociating gas. *J. Fluid Mech.* **4**, 407–425.

Gaitonde, D. 1993 Calculations on unsteady type IV interaction at Mach 8. *Wright Laboratory*, WL-TR-93-3002.

Hannemann, K., Brück, S. & Brenner, G. 1993 Numerical simulation of reacting flows related to the HEG. *19th Intl Symp. on Shock Waves, Marseille*, Vol. II (ed. R. Brun & L. Z. Dumitrescu), pp. 251–256. Springer.

Henderson, L. F. 1966 Experiments on the impingement of a supersonic jet on a flat plate. *Z. Angew Math. Phys.* **17**, 553–569.

Hiers, R. S. & Loubsky, W. J. 1967 Effects of shock-wave impingement on the heat transfer on a cylindrical leading edge. *NASA TN* D-3859.

Hornung, H. G. 1972 Non-equilibrium dissociating nitrogen flow over spheres and circular cylinders. *J. Fluid Mech.* **53**, 149–176.

Hornung, H. G. 1986 Regular and Mach reflection of shock waves. *Annu. Rev. Fluid Mech.* **18**, 33–58.

Hornung, H. G., Oertel, H. & Sandeman, R. J. 1979 Transition to Mach reflexion of shock waves in steady and pseudosteady flow with and without relaxation. *J. Fluid Mech.* **90**, 541–560.

Hornung, H. G. & Smith, G. H. 1979 The influence of relaxation on shock detachment. *J. Fluid Mech.* **93**, 225–239.

Hornung, H. G., Sturtevant, B., Belanger, J., Sanderson, S. R., Brouillette, M. & Jenkins, M. 1991 Performance data of the new free-piston shock tunnel T5 at GALCIT. *18th Intl Symp. on Shock Waves, Sendai*, Vol. I (ed. K. Takayama), pp. 603–610. Springer.

Keyes, J. W. & Hains, F. D. 1973 Analytical and experimental studies of shock interference heating in hypersonic flows. *NASA TN* D-7139.

Korkegi, R. H. 1971 Survey of viscous interactions associated with high Mach number flight. *AIAA J* **9**, 771–784.

KORTZ, S. 1993 Zum Einflußder Stickstoffdissoziation auf die Wechselwirkung zwischen Stoßwellen in Hochenthalpieströmungen. *DLR-Forschungsbericht* 93-57.

KORTZ, S., MCINTYRE, T. J. & EITELBERG, G. 1993 Experimental investigation of shock on shock interactions in the high enthalpy shock tunnel Göttingen (HEG). *19th Intl Symp. on Shock Waves*, *Marseille*, Vol. I (ed. R. Brun & L. Z. Dumitrescu), pp. 75–80. Springer.

LIGHTHILL, M. J. 1957 Dynamics of a dissociating gas. Part 1. Equilibrium flow. *J. Fluid Mech.* **2**, 1–32.

LIND, C. A. & LEWIS, M. J. 1995 Unsteady characteristics of a hypersonic Type IV shock interaction. *J. Aircraft* **32**, 1286–1293.

LIND, C. A. & LEWIS, M. J. 1996 Computational analysis of the unsteady type IV shock interaction of blunt body flows. *J. Prop. Power* **12**, 127–133.

MERZKIRCH, W. 1974 *Flow Visualization*. Academic.

MOECKEL, W. E. 1949 *Approximate method for predicting form and location of detached shock waves ahead of plane or axially symmetric bodies. NACA TN* 1921.

NONWEILER, T. R. F. 1959 Aerodynamic problems of manned space vehicles. *J. R. Aeronauti. Soc.* **63**, 521–528.

PAULL, A. 1996 A simple shock tunnel driver gas detector. *Shock Waves* **6**, 309–312.

SANDERSON, S. R. 1995 Shock wave interaction in hypervelocity flow. PhD Thesis, California Institute of Technology.

SANDERSON, S. R. HORNUNG, H. G. & STURTEVANT, B. 2003 Aspects of planar, oblique and interacting shock waves in an ideal dissociating gas. *Phys. Fluids* **15**, 1638–1649.

SANDERSON, S. R. & STURTEVANT, B. 2002 Transient heat flux measurement using a surface junction thermocouple. *Rev. Sci. Instrum.* **73**, 2781–2787.

STALKER, R. J. 1967 A study of the free piston shock tunnel. *AIAA J.* **5**, 2160–2165.

SUDANI, N. & HORNUNG, H. G. 1998 Gasdynamical detectors of driver gas contamination in a high-enthalpy shock tunnel *AIAA J.* **36**, 313–319.

SUDANI, N., VALIFERDOWSI, B. & HORNUNG, H. G. 2000 Test time increase by delaying driver gas contamination for reflected Shock tunnels. *AIAA J.* **38**, 1497–1503.

SYKES, D. M. 1962 The supersonic and low-speed flows past circular cylinders of finite length supported at one end. *J. Fluid Mech.* **12**, 367–387.

TANNEHILL, J. C., HOLST, T. L. & RAKICH, J. V. 1976 Numerical computation of two dimensional viscous blunt body flows with an impinging shock. *AIAA J.* **14**, 204–211.

WEN, C. Y. 1994 Hypervelocity flow over spheres. PhD Thesis, California Institute of Technology.

WHITE, F. M. 1974 *Viscous Fluid Flow*. McGraw-Hill.

WIETING, A. R. & HOLDEN, M. S. 1989 Experimental shock wave interference heating on a cylinder at Mach 6 and 8. *AIAA J.* **27**, 1557–1565.

ZHONG, X. 1994 Application of essentially non-oscillatory schemes to unsteady hypersonic shock-shock interference heating problems. *AIAA J.* **32**, 1606–1616.